



Angular analysis and differential branching fraction of the decay

$$B_s^0 \rightarrow \phi \mu^+ \mu^-$$

The LHCb collaboration[†]

Abstract

An angular analysis and a measurement of the differential branching fraction of the decay $B_s^0 \rightarrow \phi \mu^+ \mu^-$ are presented, using data corresponding to an integrated luminosity of 3.0 fb^{-1} of pp collisions recorded by the LHCb experiment at $\sqrt{s} = 7$ and 8 TeV. Measurements are reported as a function of q^2 , the square of the dimuon invariant mass and results of the angular analysis are found to be consistent with the Standard Model. In the range $1 < q^2 < 6 \text{ GeV}^2/c^4$, where precise theoretical calculations are available, the differential branching fraction is found to be 3.5σ below the Standard Model predictions.

Submitted to JHEP

© CERN on behalf of the LHCb collaboration, licence CC-BY-4.0.

[†]Authors are listed at the end of this paper.

1 Introduction

The decay $B_s^0 \rightarrow \phi \mu^+ \mu^-$ is mediated by a $b \rightarrow s$ flavour changing neutral current (FCNC) transition. In the Standard Model (SM) it is forbidden at tree-level and proceeds via loop diagrams as shown in Fig. 1. In extensions of the SM, new heavy particles can appear in competing diagrams and affect both the branching fraction of the decay and the angular distributions of the final-state particles.

This decay channel was first observed and studied by the CDF collaboration [1, 2] and subsequently studied by the LHCb collaboration using data collected during 2011, corresponding to an integrated luminosity of 1.0 fb^{-1} [3]. While the angular distributions were found to be in good agreement with SM expectations, the measured branching fraction differs from the recently updated SM prediction by 3.1σ [4, 5]. A similar trend is also seen for the branching fractions of other $b \rightarrow s \mu^+ \mu^-$ processes, which tend to be lower than SM predictions [6–8].

This paper presents an updated analysis of the decay $B_s^0 \rightarrow \phi(\rightarrow K^+ K^-) \mu^+ \mu^-$ using data collected by LHCb in pp collisions, corresponding to an integrated luminosity of 1.0 fb^{-1} collected during 2011 at 7 TeV and 2.0 fb^{-1} collected during 2012 at 8 TeV centre-of-mass energy. The differential branching fraction $d\mathcal{B}(B_s^0 \rightarrow \phi \mu^+ \mu^-)/dq^2$ is determined as a function of q^2 , the square of the dimuon invariant mass. In addition, a three-dimensional angular analysis in $\cos \theta_l$, $\cos \theta_K$ and Φ is performed in bins of q^2 . Here, the angle θ_K (θ_l) denotes the angle of the K^- (μ^-) with respect to the direction of flight of the B_s^0 meson in the $K^+ K^-$ ($\mu^+ \mu^-$) centre-of-mass frame, and Φ denotes the angle between the $\mu^+ \mu^-$ and the $K^+ K^-$ decay planes in the B_s^0 meson centre-of-mass frame. Compared to the previously published fit of the one-dimensional projections of the decay angles [3], the full three-dimensional angular fit gives improved sensitivity and allows access to more angular observables.

The decay $B_s^0 \rightarrow \phi \mu^+ \mu^-$ is closely related to the decay $B^0 \rightarrow K^{*0} \mu^+ \mu^-$, which has been studied extensively by LHCb [6, 9, 10]. Although B_s^0 meson production is suppressed with respect to the B^0 meson by the fragmentation fraction ratio $f_s/f_d \sim 1/4$, the narrow ϕ resonance allows a clean selection with low background levels. Furthermore, the contribution from the S wave, where the $K^+ K^-$ system is in a spin-0 configuration, is expected to be low [11]. Since the $K^+ K^- \mu^+ \mu^-$ final state is not flavour-specific, the angular observables accessible in the decay $B_s^0 \rightarrow \phi \mu^+ \mu^-$ are the CP averages F_L , $S_{3,4,7}$ and the CP asymmetries $A_{5,6,8,9}$ [12]. The flavour-averaged differential decay rate, as a function of the decay angles in bins of q^2 , is given by

$$\begin{aligned} \frac{1}{d\Gamma/dq^2} \frac{d^3\Gamma}{d\cos\theta_l d\cos\theta_K d\Phi} &= \frac{9}{32\pi} \left[\frac{3}{4}(1 - F_L) \sin^2 \theta_K + F_L \cos^2 \theta_K \right. \\ &+ \frac{1}{4}(1 - F_L) \sin^2 \theta_K \cos 2\theta_l - F_L \cos^2 \theta_K \cos 2\theta_l \\ &+ S_3 \sin^2 \theta_K \sin^2 \theta_l \cos 2\Phi + S_4 \sin 2\theta_K \sin 2\theta_l \cos \Phi \\ &+ A_5 \sin 2\theta_K \sin \theta_l \cos \Phi + A_6 \sin^2 \theta_K \cos \theta_l \\ &+ S_7 \sin 2\theta_K \sin \theta_l \sin \Phi + A_8 \sin 2\theta_K \sin 2\theta_l \sin \Phi \\ &\left. + A_9 \sin^2 \theta_K \sin^2 \theta_l \sin 2\Phi \right]. \end{aligned} \quad (1)$$

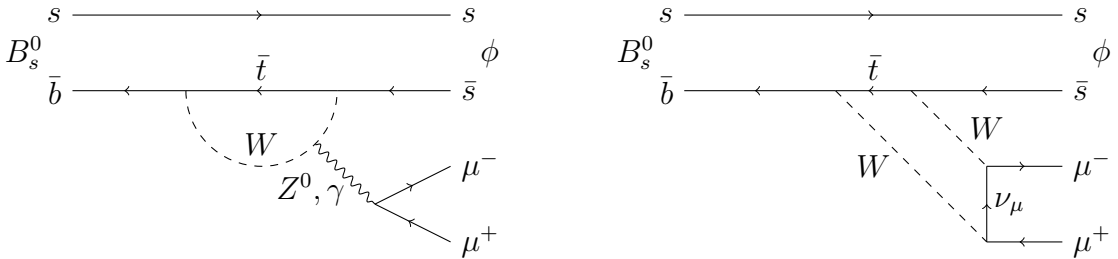


Figure 1: Examples of $b \rightarrow s$ loop diagrams contributing to the decay $B_s^0 \rightarrow \phi \mu^+ \mu^-$ in the SM.

The T -odd CP asymmetries A_8 and A_9 are predicted to be close to zero in the SM and are of particular interest, as they can be large in the presence of contributions beyond the SM [12].

2 Detector and simulation

The LHCb detector [13,14] is a single-arm forward spectrometer covering the pseudorapidity range $2 < \eta < 5$, designed for the study of particles containing b or c quarks. The detector includes a high-precision tracking system consisting of a silicon-strip vertex detector surrounding the pp interaction region, a large-area silicon-strip detector located upstream of a dipole magnet with a bending power of about 4 Tm, and three stations of silicon-strip detectors and straw drift tubes placed downstream of the magnet. The tracking system provides a measurement of momentum, p , of charged particles with a relative uncertainty that varies from 0.5% at low momentum to 1.0% at 200 GeV/ c . The minimum distance of a track to a primary vertex, the impact parameter (IP), is measured with a resolution of $(15 + 29/p_T) \mu\text{m}$, where p_T is the component of the momentum transverse to the beam, in GeV/ c . Different types of charged hadrons are distinguished using information from two ring-imaging Cherenkov detectors. Photons, electrons and hadrons are identified by a calorimeter system consisting of scintillating-pad and preshower detectors, an electromagnetic calorimeter and a hadronic calorimeter. Muons are identified by a system composed of alternating layers of iron and multiwire proportional chambers. The online event selection is performed by a trigger [15], which consists of a hardware stage, based on information from the calorimeter and muon systems, followed by a software stage, which applies a full event reconstruction.

Simulated signal samples are used to determine the effect of the detector geometry, trigger, reconstruction and selection on the signal efficiency. In addition, simulated background samples are used to determine the pollution from specific background processes. In the simulation, pp collisions are generated using PYTHIA [16] with a specific LHCb configuration [17]. Decays of hadronic particles are described by EVTGEN [18], in which final-state radiation is generated using PHOTOS [19]. The interaction of the generated particles with the detector, and its response, are implemented using the GEANT4 toolkit [20]

as described in Ref. [21]. Data-driven corrections are applied to the simulated samples to account for imperfect modelling of particle identification performance, the B_s^0 meson transverse momentum spectrum and B_s^0 vertexing quality, as well as track multiplicity.

3 Selection of signal candidates

The $B_s^0 \rightarrow \phi\mu^+\mu^-$ signal candidates are required to satisfy the hardware trigger requirement, which selects muons with $p_T > 1.48 \text{ GeV}/c$ in the 7 TeV data and $p_T > 1.76 \text{ GeV}/c$ in the 8 TeV data. In the subsequent software trigger, at least one of the final-state particles is required to have both $p_T > 0.8 \text{ GeV}/c$ and IP larger than $100 \mu\text{m}$ with respect to all of the primary pp interaction vertices (PVs) in the event. The tracks of two or more of the final-state particles are also required to form a vertex that is significantly displaced from any PV.

Signal candidates are accepted if their reconstructed invariant mass is in the range $5100 < m(K^+K^-\mu^+\mu^-) < 5800 \text{ MeV}/c^2$ and the invariant mass of the K^+K^- system is within $12 \text{ MeV}/c^2$ of the known ϕ mass [22]. The final-state particles are required to have significant χ_{IP}^2 with respect to any PV in the event, where χ_{IP}^2 denotes the change in the χ^2 of the PV when reconstructed with or without the considered track. The four final-state tracks are then fitted to a common vertex which is required to be of good quality and significantly displaced from any PV in the event. The signal candidate is required to have small χ_{IP}^2 with respect to a PV in the event. Furthermore, the angle θ_{DIRA} between the reconstructed B_s^0 momentum and the vector connecting the PV with the decay vertex is required to be small.

To further reduce the combinatorial background, a boosted decision tree (BDT) [23] using the AdaBoost algorithm [24] is employed. The BDT is trained with a sample of $B_s^0 \rightarrow J/\psi(\rightarrow \mu^+\mu^-)\phi(\rightarrow K^+K^-)$ decays as a signal proxy and events from the upper mass sideband, $5567 < m(K^+K^-\mu^+\mu^-) < 5800 \text{ MeV}/c^2$, as a proxy for the background. The discriminating variables of the BDT are the χ_{IP}^2 of the B_s^0 signal candidate and all final-state tracks, the B_s^0 transverse momentum, the χ^2 of the vertex fit (χ_{Vtx}^2), the flight distance significance of the signal candidate, and particle identification information for the final-state particles. The BDT selection has an efficiency of 96% for signal events with a background rejection of 95%.

The reconstructed B_s^0 mass versus q^2 for signal candidates after the full selection is given in Fig. 2. The signal decay $B_s^0 \rightarrow \phi\mu^+\mu^-$ is clearly visible as a vertical band. In the q^2 region around the J/ψ and $\psi(2S)$ masses, the tree-level charmonium decays $B_s^0 \rightarrow J/\psi\phi$ and $B_s^0 \rightarrow \psi(2S)\phi$ dominate. The decay $B_s^0 \rightarrow J/\psi\phi$ is used as a control mode throughout the analysis.

3.1 Backgrounds

The decays $B_s^0 \rightarrow J/\psi\phi$ and $B_s^0 \rightarrow \psi(2S)\phi$, primarily originating from $b \rightarrow c\bar{c}s$ tree-level processes, are vetoed by rejecting candidates in the q^2 regions $8.0 < q^2 < 11.0 \text{ GeV}^2/c^4$

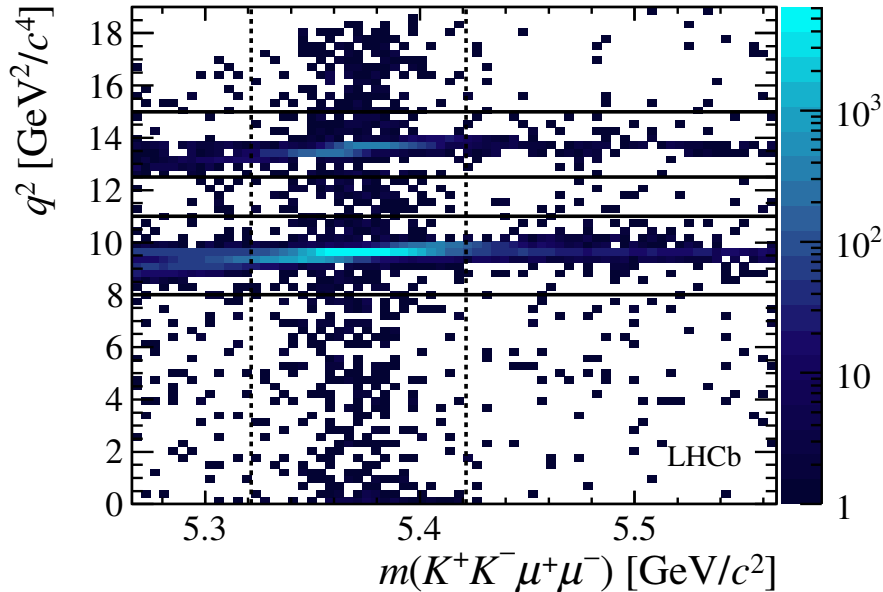


Figure 2: Two-dimensional distribution of q^2 versus the invariant mass of the $K^+K^-\mu^+\mu^-$ system. The signal decay $B_s^0 \rightarrow \phi\mu^+\mu^-$ is clearly visible within the $\pm 50 \text{ MeV}/c^2$ interval around the B_s^0 mass, indicated by the dashed vertical lines. The horizontal lines denote the charmonium regions, where the tree-level decays $B_s^0 \rightarrow J/\psi\phi$ and $B_s^0 \rightarrow \psi(2S)\phi$ dominate.

and $12.5 < q^2 < 15.0 \text{ GeV}^2/c^4$. The $B_s^0 \rightarrow J/\psi\phi$ decay can also constitute a peaking background if one of the final-state muons is misidentified as a kaon and vice-versa. This background is vetoed by rejecting candidates for which the invariant mass of the $K^\pm\mu^\mp$ system, with the kaon reconstructed under the muon mass hypothesis, is within $45 \text{ MeV}/c^2$ of the known J/ψ meson mass [22], unless the final-state particles fulfil stringent particle identification requirements. After the veto is applied, this background contribution is found to be negligible.

The rare baryonic decay $\Lambda_b^0 \rightarrow \Lambda(1520)(\rightarrow pK^-)\mu^+\mu^-$ can mimic the signal decay if the proton in the final state is misidentified as a kaon. This potential background is vetoed by rejecting events with invariant mass close to the known Λ_b^0 baryon mass [22] where one kaon has the proton mass hypothesis assigned, unless the kaon passes stringent particle identification requirements. Assuming a q^2 dependence following Ref. [25] and using $\mathcal{B}(\Lambda_b^0 \rightarrow \Lambda\mu^+\mu^-) = (0.96 \pm 0.29) \times 10^{-6}$ [26] as an estimate for the unknown $\Lambda_b^0 \rightarrow \Lambda(1520)\mu^+\mu^-$ branching fraction, a yield of 2.0 ± 0.8 $\Lambda_b^0 \rightarrow \Lambda(1520)\mu^+\mu^-$ background events is expected in the signal region, within $50 \text{ MeV}/c^2$ of the known B_s^0 mass [22], after the veto. The rare decay $B^0 \rightarrow K^{*0}\mu^+\mu^-$ can be a peaking background if the pion in the final state is reconstructed as a kaon. After suppressing this background using particle identification information, a yield of 1.7 ± 0.4 events is expected in the signal region. The background pollution from $\Lambda_b^0 \rightarrow \Lambda(1520)\mu^+\mu^-$ and $B^0 \rightarrow K^{*0}\mu^+\mu^-$ decays is neglected in the fit and treated as a systematic uncertainty. Backgrounds from

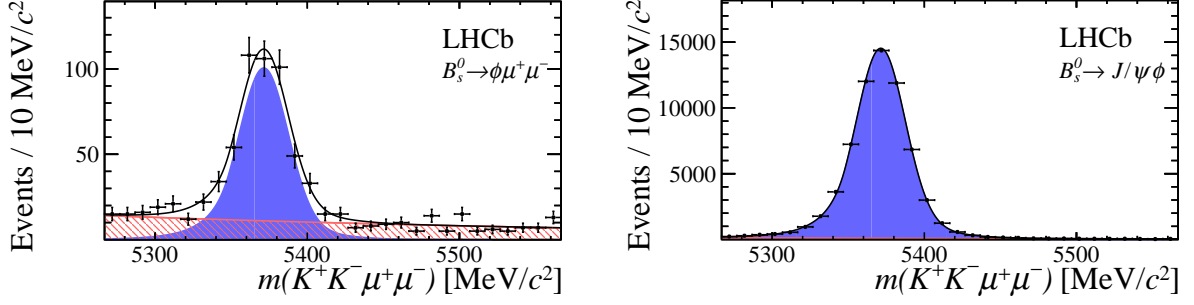


Figure 3: Invariant mass distribution for (left) $B_s^0 \rightarrow \phi \mu^+ \mu^-$ signal decays, integrated over the q^2 bins used, and for (right) the control mode $B_s^0 \rightarrow J/\psi \phi$ in the $K^+ K^- \mu^+ \mu^-$ final state. The signal component is given by the solid blue area, the background component by the shaded red area.

semileptonic $b \rightarrow c(\rightarrow s\mu^-\bar{\nu}_\mu)\mu^+\nu_\mu$ cascade decays and fully hadronic decays such as $B_s^0 \rightarrow D_s^-(\rightarrow K^+K^-\pi^-)\pi^+$, where hadrons are misidentified as muons, are estimated to be small and can therefore be neglected.

4 Differential branching fraction

Figure 3 shows the $K^+K^-\mu^+\mu^-$ invariant mass distribution for the $B_s^0 \rightarrow \phi \mu^+ \mu^-$ signal decay integrated over q^2 , as well as for the control mode $B_s^0 \rightarrow J/\psi \phi$. To determine the $B_s^0 \rightarrow \phi \mu^+ \mu^-$ signal yields in bins of q^2 , extended maximum likelihood fits are performed. The combinatorial background is described by an exponential function, whilst the signal component is modelled with the sum of two Gaussian functions with a common mean and a radiative power-law tail toward smaller invariant mass values. The parameters describing the signal mass shape are determined from a fit to the $B_s^0 \rightarrow J/\psi \phi$ control mode. The q^2 dependence of the signal mass resolution is accounted for by using scale factors, which are determined from simulation. The $K^+K^-\mu^+\mu^-$ invariant mass distributions for the signal decay in bins of q^2 are given in Appendix A; the yields and corresponding uncertainties are listed in Table 1. Integrating over the q^2 bins, the signal yield is found to be 432 ± 24 . A fit to the control mode $B_s^0 \rightarrow J/\psi \phi$, which is used for normalisation, gives $N_{J/\psi \phi} = 62\,033 \pm 260$ decays.

The differential branching fraction for a given q^2 bin $[q_{\min}^2, q_{\max}^2]$ is calculated according to

$$\frac{d\mathcal{B}(B_s^0 \rightarrow \phi \mu^+ \mu^-)}{dq^2} = \frac{1}{q_{\max}^2 - q_{\min}^2} \cdot \frac{N_{\phi\mu\mu}}{N_{J/\psi\phi}} \cdot \frac{\epsilon_{J/\psi\phi}}{\epsilon_{\phi\mu\mu}} \cdot \mathcal{B}(B_s^0 \rightarrow J/\psi \phi) \mathcal{B}(J/\psi \rightarrow \mu^+ \mu^-), \quad (2)$$

where $N_{\phi\mu\mu}$ and $N_{J/\psi\phi}$ denote the yield of the signal and normalisation mode, and $\epsilon_{\phi\mu\mu}$ and $\epsilon_{J/\psi\phi}$ their respective efficiencies. The branching fractions are given by $\mathcal{B}(J/\psi \rightarrow \mu^+ \mu^-) = (5.961 \pm 0.033) \times 10^{-2}$ [22] and $\mathcal{B}(B_s^0 \rightarrow J/\psi \phi) = (10.76 \pm 0.81) \times 10^{-4}$. For the branching fraction of the normalisation channel $B_s^0 \rightarrow J/\psi \phi$ the LHCb measurement [11]

is recalculated using an updated measurement of $f_s/f_d = 0.259 \pm 0.015$ [27]. A weighted average is calculated by combining this updated measurement with the measurements by Belle [28] and CDF [29]. The resulting relative and absolute differential branching fractions are given in Table 1. The differential branching fraction is also shown in Fig. 4, overlaid with SM predictions from Refs. [4, 5]. In the q^2 region $1.0 < q^2 < 6.0 \text{ GeV}^2/c^4$ the measured differential branching fraction lies 3.5σ below the SM expectation of $(4.81 \pm 0.51) \times 10^{-8} \text{ GeV}^{-2} c^4$ [4]. For the SM predictions, the form factors are determined in a combined fit to the results of light-cone sum rule calculations at low q^2 [5] and lattice QCD calculations at high q^2 [30, 31]. Owing to their proximity to the charmonium resonances, no prediction is available corresponding to the q^2 bins $5.0 < q^2 < 8.0 \text{ GeV}^2/c^4$ and $11.0 < q^2 < 12.5 \text{ GeV}^2/c^4$.

The total branching fraction of the signal decay is given by the integral over the six q^2 bins. To account for the fraction of signal events in the vetoed q^2 regions, a correction factor $f_{\text{veto}} = 1.520 \pm 0.003 \pm 0.043$ is applied, which is determined using the calculation in Ref. [32] with updated form factors from Ref. [33]. The first given uncertainty is statistical, the second is systematic.

The resulting relative and total branching fractions are

$$\frac{\mathcal{B}(B_s^0 \rightarrow \phi \mu^+ \mu^-)}{\mathcal{B}(B_s^0 \rightarrow J/\psi \phi)} = (7.41_{-0.40}^{+0.42} \pm 0.20 \pm 0.21) \times 10^{-4},$$

$$\mathcal{B}(B_s^0 \rightarrow \phi \mu^+ \mu^-) = (7.97_{-0.43}^{+0.45} \pm 0.22 \pm 0.23 \pm 0.60) \times 10^{-7},$$

where the uncertainties are (from left to right) statistical, systematic, and from the extrapolation to the full q^2 region. For the total branching fraction, a further uncertainty originates from the uncertainty on the branching fraction of the normalisation mode.

4.1 Systematic uncertainties

For the branching fraction ratio $\mathcal{B}(B_s^0 \rightarrow \phi \mu^+ \mu^-)/\mathcal{B}(B_s^0 \rightarrow J/\psi \phi)$, systematic uncertainties are mostly due to uncertainties on the efficiency ratio $\epsilon_{J/\psi \phi}/\epsilon_{\phi \mu \mu}$, which is taken from simulation. To evaluate the size of uncertainties affecting the efficiency ratio, it is recalculated after applying the corresponding systematic variation to the simulated samples. The observed deviation is taken as systematic uncertainty. The procedure to correct the tracking efficiency in simulation introduces a systematic uncertainty on the efficiency ratio of less than 0.6%. The correction to particle identification performance in simulation has a systematic uncertainty of 0.5%. The relative efficiency is further affected by the data-driven corrections to the simulation in the distribution of the variables $p_T(B_s^0)$ and $\chi_{\text{Vtx}}^2(B_s^0)$, as well as the track multiplicity, which have a combined systematic effect of 1.0%. The non-uniform angular acceptance detailed in Sec. 5 introduces a dependence of the signal efficiency on the underlying physics model. Its effect on the branching fraction measurement is evaluated by varying the Wilson coefficients used in the generation of simulated signal events and is found to be less than 1.6%. The selection requirements introduce a decay-time dependence of the efficiencies which can, due to the sizeable lifetime difference in the B_s^0 system [34], affect the measured branching fraction [35]. The

Table 1: The signal yields for $B_s^0 \rightarrow \phi\mu^+\mu^-$ decays, as well as the differential branching fraction relative to the normalisation mode and the absolute differential branching fraction, in bins of q^2 . The given uncertainties are (from left to right) statistical, systematic, and the uncertainty on the branching fraction of the normalisation mode.

q^2 bin [GeV^2/c^4]	$N_{\phi\mu\mu}$	$\frac{d\mathcal{B}(B_s^0 \rightarrow \phi\mu\mu)}{\mathcal{B}(B_s^0 \rightarrow J/\psi\phi)dq^2}$ [$10^{-5} \text{ GeV}^{-2} c^4$]	$\frac{d\mathcal{B}(B_s^0 \rightarrow \phi\mu^+\mu^-)}{dq^2}$ [$10^{-8} \text{ GeV}^{-2} c^4$]
$0.1 < q^2 < 2.0$	$85.2^{+10.6}_{-10.0}$	$5.44^{+0.68}_{-0.64} \pm 0.13$	$5.85^{+0.73}_{-0.69} \pm 0.14 \pm 0.44$
$2.0 < q^2 < 5.0$	$59.6^{+9.8}_{-9.2}$	$2.38^{+0.39}_{-0.37} \pm 0.06$	$2.56^{+0.42}_{-0.39} \pm 0.06 \pm 0.19$
$5.0 < q^2 < 8.0$	$82.7^{+11.5}_{-10.9}$	$2.98^{+0.41}_{-0.39} \pm 0.07$	$3.21^{+0.44}_{-0.42} \pm 0.08 \pm 0.24$
$11.0 < q^2 < 12.5$	$70.4^{+10.4}_{-9.8}$	$4.37^{+0.64}_{-0.61} \pm 0.14$	$4.71^{+0.69}_{-0.65} \pm 0.15 \pm 0.36$
$15.0 < q^2 < 17.0$	$83.1^{+10.4}_{-9.9}$	$4.20^{+0.53}_{-0.50} \pm 0.11$	$4.52^{+0.57}_{-0.54} \pm 0.12 \pm 0.34$
$17.0 < q^2 < 19.0$	$54.2^{+7.8}_{-7.4}$	$3.68^{+0.53}_{-0.50} \pm 0.13$	$3.96^{+0.57}_{-0.54} \pm 0.14 \pm 0.30$
$1.0 < q^2 < 6.0$	$101.0^{+12.8}_{-12.2}$	$2.40^{+0.30}_{-0.29} \pm 0.07$	$2.58^{+0.33}_{-0.31} \pm 0.08 \pm 0.19$
$15.0 < q^2 < 19.0$	$135.5^{+13.2}_{-12.7}$	$3.75^{+0.37}_{-0.35} \pm 0.12$	$4.04^{+0.39}_{-0.38} \pm 0.13 \pm 0.30$

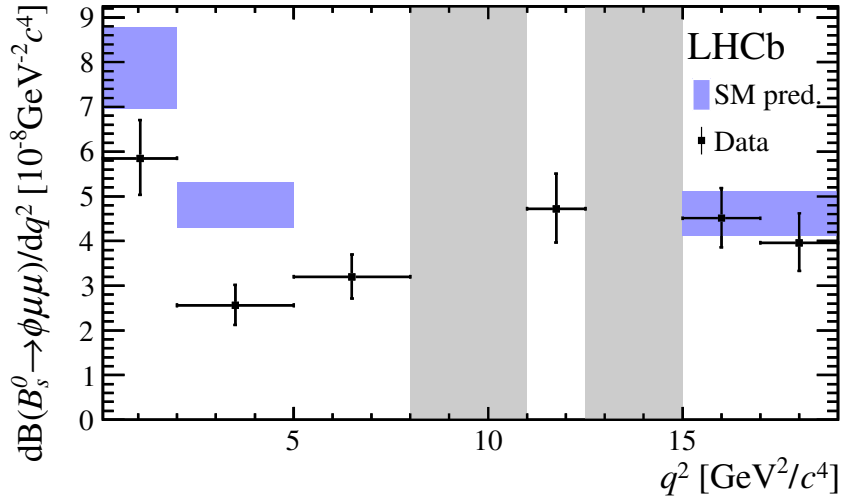


Figure 4: Differential branching fraction of the decay $B_s^0 \rightarrow \phi\mu^+\mu^-$, overlaid with SM predictions [4, 5] indicated by blue shaded boxes. The vetoes excluding the charmonium resonances are indicated by grey areas.

systematic uncertainty is determined with simulated $B_s^0 \rightarrow \phi\mu^+\mu^-$ signal events, generated using time-dependent decay amplitudes as described in Ref. [12]. When varying the Wilson coefficients, the size of the effect is found to be at most 1.6%, which is taken as the

Table 2: Systematic uncertainties [$10^{-5} \text{ GeV}^{-2} c^4$] on the branching fraction ratio $d\mathcal{B}(B_s^0 \rightarrow \phi\mu^+\mu^-)/\mathcal{B}(B_s^0 \rightarrow J/\psi\phi)dq^2$ per bin of q^2 [GeV^2/c^4].

Source	[0.1, 2]	[2, 5]	[5, 8]	[11, 12.5]	[15, 17]	[17, 19]	[1, 6]	[15, 19]
Simulation corr.	0.01	0.01	0.01	0.01	0.05	0.04	0.00	0.04
Angular model	0.04	0.00	0.01	0.00	0.01	0.06	0.00	0.01
Efficiency ratio	0.06	0.03	0.03	0.06	0.06	0.07	0.02	0.04
Signal mass model	0.02	0.01	0.03	0.03	0.03	0.00	0.05	0.05
Bkg. mass model	0.02	0.02	0.02	0.02	0.03	0.05	0.01	0.06
Time acceptance	0.09	0.04	0.05	0.07	0.07	0.06	0.04	0.06
$\mathcal{B}(J/\psi \rightarrow \mu^+\mu^-)$	0.03	0.01	0.02	0.02	0.02	0.02	0.01	0.02
Peaking bkg.	0.03	0.02	0.02	0.10	0.02	0.01	0.02	0.01
Quadratic sum	0.13	0.06	0.07	0.14	0.11	0.13	0.07	0.12

systematic uncertainty. The statistical uncertainty due to the limited size of the simulated signal samples leads to a systematic uncertainty of 1.9%.

The systematic uncertainties due to the parametrisation of the mass shapes are evaluated using pseudoexperiments. For the signal mass model, events are generated using a double Gaussian mass shape, and then fitted using both the double Gaussian as well as the nominal signal mass shape, taking the observed deviation as the systematic uncertainty. For the parametrisation of the combinatorial background, the nominal exponential function is compared with a linear mass model. The systematic uncertainties due to the modelling of the signal and background mass shape are 2.1% and 1.6%, respectively. Peaking backgrounds are neglected in the fit for determination of the signal yields. The main sources of systematic uncertainty are caused by contributions from the decays $\Lambda_b^0 \rightarrow pK^-\mu^+\mu^-$ and $B^0 \rightarrow K^{*0}\mu^+\mu^-$, resulting in systematic uncertainties of 0.2 – 2.2%, depending on the q^2 bin. Finally, the uncertainty on the branching fraction of the decay $J/\psi \rightarrow \mu^+\mu^-$ amounts to a systematic uncertainty of 0.6%. The complete list of systematic uncertainties is given in Table 2.

For the total branching fraction of the signal decay, the uncertainty on the branching fraction of the normalisation channel is the dominant systematic uncertainty, at 7.5%. The uncertainty on the correction factor f_{veto} to account for signal events that are rejected by the charmonium vetoes is estimated by varying the Wilson coefficients and form-factor parameters, leading to a systematic uncertainty of 2.9%.

5 Angular analysis

For the determination of the four CP averages F_L , $S_{3,4,7}$ and the four CP asymmetries $A_{5,6,8,9}$ an unbinned maximum likelihood fit to the three-dimensional angular distribution and the $K^+K^-\mu^+\mu^-$ invariant mass distribution is performed in each q^2 bin. The models described in Sec. 4 are used to parametrise the mass line shapes for signal and background. The angular distribution of the signal component is given by Eq. 1. The angular background distribution is described by the product of second-order Chebyshev polynomials in the three decay angles.

The non-uniform efficiency due to the reconstruction, triggering and selection of signal candidates distorts the angular distributions of the final-state particles, as well as the q^2 distribution. This acceptance effect is parametrised using Legendre polynomials, according to

$$\epsilon(\cos\theta_l, \cos\theta_K, \Phi, q^2) = \sum_{klmn} c_{klmn} P_k(\cos\theta_l) P_l(\cos\theta_K) P_m(\Phi) P_n(q^2), \quad (3)$$

where $P_i(x)$ denote Legendre polynomials of order i and c_{klmn} the coefficients that are determined by performing a moments analysis using a large sample of simulated $B_s^0 \rightarrow \phi\mu^+\mu^-$ signal events generated according to a phase-space model. The maximum order of the polynomials that is included is four for $\cos\theta_l$, two for $\cos\theta_K$, six for the angle Φ and five for q^2 . In addition, the acceptance is assumed to be symmetric in the decay angles. This choice corresponds to the lowest orders of polynomials that describe the acceptance effect. The acceptance description is cross-checked using the control mode $B_s^0 \rightarrow J/\psi\phi$. An angular analysis of the control mode is performed and the angular observables are found to be in good agreement with the previous measurement [34].

Appendix B gives the one-dimensional angular distributions of the signal decay in each q^2 bin, overlaid with the projections of the likelihood fit. For the q^2 bins with the lowest number of signal candidates, pseudoexperiments show the likelihood estimator to be biased for certain observables due to boundary effects which arise from the requirement of Eq. 1 being positive for all values of the decay angles. Therefore, the Feldman-Cousins method [36] is used to determine confidence regions for each observable, which guarantees correct coverage for low signal yields. The remaining signal observables are treated as nuisance parameters following the plugin method [37]. The Feldman-Cousins scans for the angular observables in bins of q^2 are given in Appendix C. In some q^2 bins, the shape of the obtained confidence level is dominated by effects arising from the boundary condition. Table 3 gives the minima of the Feldman-Cousins scans and the 68% confidence intervals. The linear correlations between the angular observables in the different q^2 bins are given in Appendix D. The angular observables are shown in Fig. 5, overlaid with SM predictions from Refs. [4, 5]. No predictions are given for S_7 and $A_{5,6,8,9}$; they are expected to be close to zero in the SM.

Table 3: (Top) CP -averaged angular observables F_L and $S_{3,4,7}$ and (bottom) CP asymmetries $A_{5,6,8,9}$ obtained from the unbinned maximum likelihood fit, where the first uncertainty is statistical and the second is systematic.

q^2 bin [GeV $^2/c^4$]	F_L	S_3	S_4	S_7
$0.1 < q^2 < 2.0$	$0.20^{+0.08}_{-0.09} \pm 0.02$	$-0.05^{+0.13}_{-0.13} \pm 0.01$	$0.27^{+0.28}_{-0.18} \pm 0.01$	$0.04^{+0.12}_{-0.12} \pm 0.00$
$2.0 < q^2 < 5.0$	$0.68^{+0.16}_{-0.13} \pm 0.03$	$-0.06^{+0.19}_{-0.23} \pm 0.01$	$-0.47^{+0.30}_{-0.44} \pm 0.01$	$-0.03^{+0.18}_{-0.23} \pm 0.01$
$5.0 < q^2 < 8.0$	$0.54^{+0.10}_{-0.09} \pm 0.02$	$-0.10^{+0.20}_{-0.29} \pm 0.01$	$-0.10^{+0.15}_{-0.18} \pm 0.01$	$0.04^{+0.16}_{-0.20} \pm 0.01$
$11.0 < q^2 < 12.5$	$0.29^{+0.11}_{-0.11} \pm 0.04$	$-0.19^{+0.20}_{-0.23} \pm 0.01$	$-0.47^{+0.21}_{-0.29} \pm 0.01$	$0.00^{+0.15}_{-0.17} \pm 0.01$
$15.0 < q^2 < 17.0$	$0.23^{+0.09}_{-0.08} \pm 0.02$	$-0.06^{+0.16}_{-0.19} \pm 0.01$	$-0.03^{+0.15}_{-0.15} \pm 0.01$	$0.12^{+0.16}_{-0.13} \pm 0.01$
$17.0 < q^2 < 19.0$	$0.40^{+0.13}_{-0.15} \pm 0.02$	$-0.07^{+0.23}_{-0.27} \pm 0.02$	$-0.39^{+0.25}_{-0.34} \pm 0.02$	$0.20^{+0.29}_{-0.22} \pm 0.01$
$1.0 < q^2 < 6.0$	$0.63^{+0.09}_{-0.09} \pm 0.03$	$-0.02^{+0.12}_{-0.13} \pm 0.01$	$-0.19^{+0.14}_{-0.13} \pm 0.01$	$-0.03^{+0.14}_{-0.14} \pm 0.00$
$15.0 < q^2 < 19.0$	$0.29^{+0.07}_{-0.06} \pm 0.02$	$-0.09^{+0.11}_{-0.12} \pm 0.01$	$-0.14^{+0.11}_{-0.11} \pm 0.01$	$0.13^{+0.11}_{-0.11} \pm 0.01$

q^2 bin [GeV $^2/c^4$]	A_5	A_6	A_8	A_9
$0.1 < q^2 < 2.0$	$-0.02^{+0.13}_{-0.13} \pm 0.00$	$-0.19^{+0.15}_{-0.15} \pm 0.01$	$0.10^{+0.14}_{-0.14} \pm 0.00$	$0.03^{+0.14}_{-0.14} \pm 0.01$
$2.0 < q^2 < 5.0$	$0.09^{+0.28}_{-0.22} \pm 0.01$	$0.09^{+0.20}_{-0.19} \pm 0.02$	$0.19^{+0.26}_{-0.21} \pm 0.01$	$-0.13^{+0.24}_{-0.30} \pm 0.01$
$5.0 < q^2 < 8.0$	$0.04^{+0.17}_{-0.17} \pm 0.01$	$-0.01^{+0.14}_{-0.12} \pm 0.01$	$-0.12^{+0.17}_{-0.19} \pm 0.01$	$-0.03^{+0.17}_{-0.16} \pm 0.01$
$11.0 < q^2 < 12.5$	$0.08^{+0.21}_{-0.21} \pm 0.01$	$-0.16^{+0.16}_{-0.18} \pm 0.01$	$-0.01^{+0.15}_{-0.15} \pm 0.01$	$-0.02^{+0.16}_{-0.15} \pm 0.01$
$15.0 < q^2 < 17.0$	$0.02^{+0.13}_{-0.14} \pm 0.01$	$0.01^{+0.12}_{-0.17} \pm 0.01$	$0.08^{+0.16}_{-0.18} \pm 0.01$	$0.21^{+0.18}_{-0.12} \pm 0.01$
$17.0 < q^2 < 19.0$	$0.13^{+0.29}_{-0.27} \pm 0.01$	$-0.04^{+0.18}_{-0.19} \pm 0.01$	$-0.16^{+0.24}_{-0.29} \pm 0.01$	$-0.02^{+0.19}_{-0.19} \pm 0.01$
$1.0 < q^2 < 6.0$	$0.20^{+0.13}_{-0.13} \pm 0.00$	$0.08^{+0.12}_{-0.11} \pm 0.01$	$-0.00^{+0.15}_{-0.17} \pm 0.00$	$-0.01^{+0.13}_{-0.13} \pm 0.01$
$15.0 < q^2 < 19.0$	$0.11^{+0.10}_{-0.10} \pm 0.00$	$0.00^{+0.10}_{-0.11} \pm 0.01$	$0.03^{+0.12}_{-0.12} \pm 0.00$	$0.12^{+0.11}_{-0.09} \pm 0.00$

5.1 Systematic uncertainties

The systematic uncertainties on the angular observables are evaluated using large numbers of pseudoexperiments where simulated events are generated to reflect the measured angular distributions and event yield. To reduce statistical effects, each sample is fitted twice, once with and once without systematic variations.

The angular acceptance correction, which is determined from simulation, is a significant source of systematic uncertainties for the angular observables. The data-driven corrections of the distributions of $p_T(B_s^0)$, $\chi_{\text{vtx}}^2(B_s^0)$ and track multiplicity, as well as particle identification performance and tracking efficiency, amount to a systematic uncertainty of less than 0.01 in total. Furthermore, the kinematic distributions of the final-state particles are cross-checked using the control mode $B_s^0 \rightarrow J/\psi \phi$. Correcting for kinematic differences between data and simulation amounts to a systematic deviation of less than 0.01. The effect of the limited size of the simulated signal samples on the acceptance

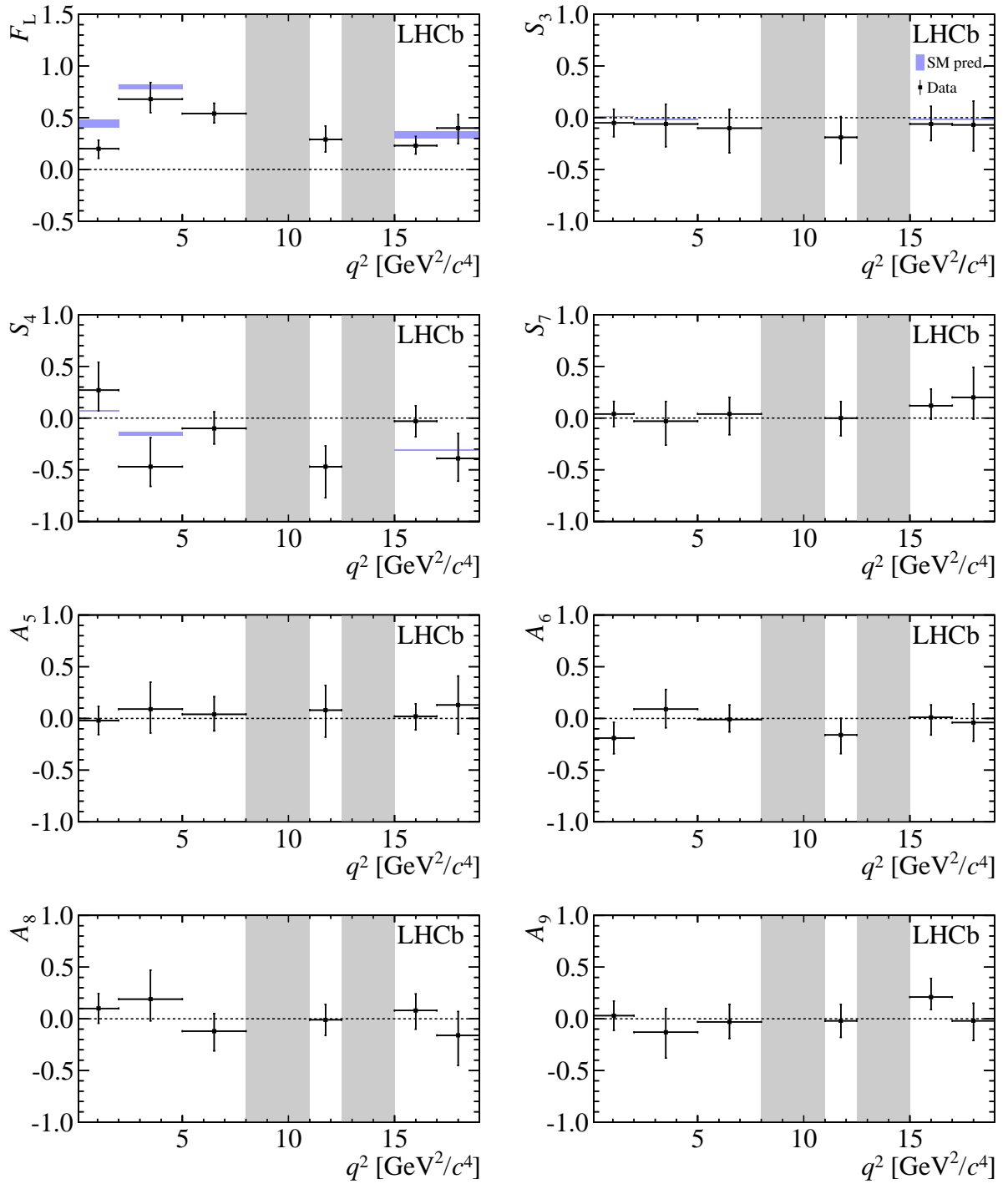


Figure 5: CP -averaged angular observables F_L and $S_{3,4,7}$ and CP asymmetries $A_{5,6,8,9}$ shown by black dots, overlaid with SM predictions [4, 5], where available, indicated as blue shaded boxes. The vetoes excluding the charmonium resonances are indicated by grey areas.

description is evaluated by varying the Legendre coefficients in Eq. 3 according to their corresponding covariance matrix. The resulting systematic uncertainty is smaller than 0.02 for all observables and q^2 bins. The four-dimensional acceptance correction is evaluated at the centre of each q^2 bin. To estimate the systematic effect due to this, an alternative acceptance description is used, where a separate three-dimensional acceptance is used for each q^2 bin. The resulting systematic deviation is negligible.

The systematic effect of neglecting peaking backgrounds is evaluated by performing toy studies, where simulated $\Lambda_b^0 \rightarrow pK^-\mu^+\mu^-$ and $B^0 \rightarrow K^{*0}\mu^+\mu^-$ background events are added, according to their expected yields for the specific q^2 bin. The resulting systematic deviations of the angular observables are smaller than 0.01 for all observables and q^2 bins. The S-wave pollution for the decay $B_s^0 \rightarrow \phi\mu^+\mu^-$ is expected to be similar to that of the $B_s^0 \rightarrow J/\psi\phi$ decay, at the level of 1.1% [11]. The effect of the S wave in the K^+K^- system on the angular observables is determined to be smaller than 0.01 using toy studies. The combinatorial background is described using second-order Chebyshev polynomials determined from the upper mass sideband. The systematic uncertainty associated with this model choice is estimated by using first-order polynomials as an alternative. With a systematic effect of up to 0.04 on the angular observables, depending on q^2 bin, this constitutes the dominant systematic uncertainty for the angular analysis. In addition, the effect of fixing the angular background parameters in the nominal fit is evaluated using toy studies. The systematic deviation is found to be smaller than 0.02 for all observables and q^2 bins.

The total systematic uncertainty, given by the quadratic sum over all systematic effects, is found to be small compared to the statistical uncertainties for all angular observables in all q^2 bins.

6 Conclusions

Measurements of the differential branching fraction and the first full three-dimensional angular analysis of the decay $B_s^0 \rightarrow \phi\mu^+\mu^-$ are presented, using data collected by the LHCb experiment in pp collisions, corresponding to an integrated luminosity of 3.0 fb^{-1} . The results are given in Tables 1 and 3 and are the most precise measurements of these quantities to date. The CP -averaged angular observables S_4 and S_7 are determined for the first time for this decay. The determination of the CP asymmetries A_5 and A_8 constitutes the first measurement of these quantities for any rare $b \rightarrow s\ell\ell$ decay, providing additional constraints to new physics models. All angular observables are found to be compatible with SM predictions.

The $B_s^0 \rightarrow \phi\mu^+\mu^-$ branching fraction relative to the normalisation mode $B_s^0 \rightarrow J/\psi\phi$ is measured to be

$$\frac{\mathcal{B}(B_s^0 \rightarrow \phi\mu^+\mu^-)}{\mathcal{B}(B_s^0 \rightarrow J/\psi\phi)} = (7.41_{-0.40}^{+0.42} \pm 0.20 \pm 0.21) \times 10^{-4},$$

and the resulting total absolute branching fraction is measured to be

$$\mathcal{B}(B_s^0 \rightarrow \phi \mu^+ \mu^-) = (7.97_{-0.43}^{+0.45} \pm 0.22 \pm 0.23 \pm 0.60) \times 10^{-7},$$

where the uncertainties are (from left to right) statistical, systematic, and from the extrapolation to the full q^2 region. For the total branching fraction, a further uncertainty originates from the uncertainty on the branching fraction of the normalisation mode. The measured branching fraction is compatible with the previous measurement [3] and lies below SM expectations. For the q^2 region $1.0 < q^2 < 6.0 \text{ GeV}^2/c^4$ the differential branching fraction of $(2.58_{-0.31}^{+0.33} \pm 0.08 \pm 0.19) \times 10^{-8} \text{ GeV}^{-2}c^4$ is 3.5σ below the SM prediction of $(4.81 \pm 0.51) \times 10^{-8} \text{ GeV}^{-2}c^4$ [4, 5].

Acknowledgements

We express our gratitude to our colleagues in the CERN accelerator departments for the excellent performance of the LHC. We thank the technical and administrative staff at the LHCb institutes. We acknowledge support from CERN and from the national agencies: CAPES, CNPq, FAPERJ and FINEP (Brazil); NSFC (China); CNRS/IN2P3 (France); BMBF, DFG, HGF and MPG (Germany); INFN (Italy); FOM and NWO (The Netherlands); MNiSW and NCN (Poland); MEN/IFA (Romania); MinES and FANO (Russia); MinECo (Spain); SNSF and SER (Switzerland); NASU (Ukraine); STFC (United Kingdom); NSF (USA). The Tier1 computing centres are supported by IN2P3 (France), KIT and BMBF (Germany), INFN (Italy), NWO and SURF (The Netherlands), PIC (Spain), GridPP (United Kingdom). We are indebted to the communities behind the multiple open source software packages on which we depend. We are also thankful for the computing resources and the access to software R&D tools provided by Yandex LLC (Russia). Individual groups or members have received support from EPLANET, Marie Skłodowska-Curie Actions and ERC (European Union), Conseil général de Haute-Savoie, Labex ENIGMASS and OCEVU, Région Auvergne (France), RFBR (Russia), XuntaGal and GENCAT (Spain), Royal Society and Royal Commission for the Exhibition of 1851 (United Kingdom).

Appendices

A Invariant mass distributions

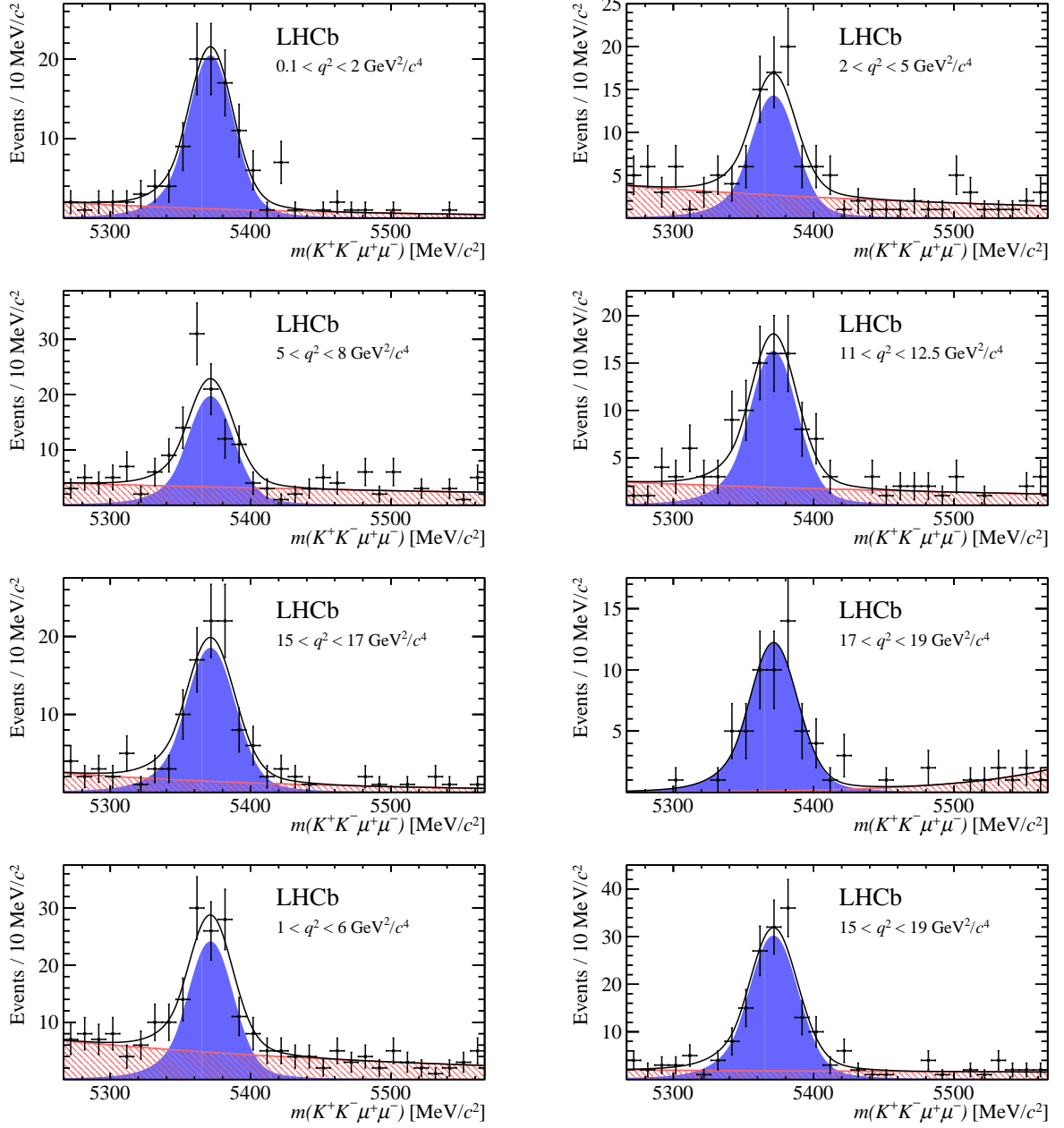


Figure 6: Invariant mass distributions for $B_s^0 \rightarrow \phi \mu^+ \mu^-$ signal decays in bins of q^2 . The signal component is shown by the solid blue area, the background component by the shaded red area.

B Angular fit projections

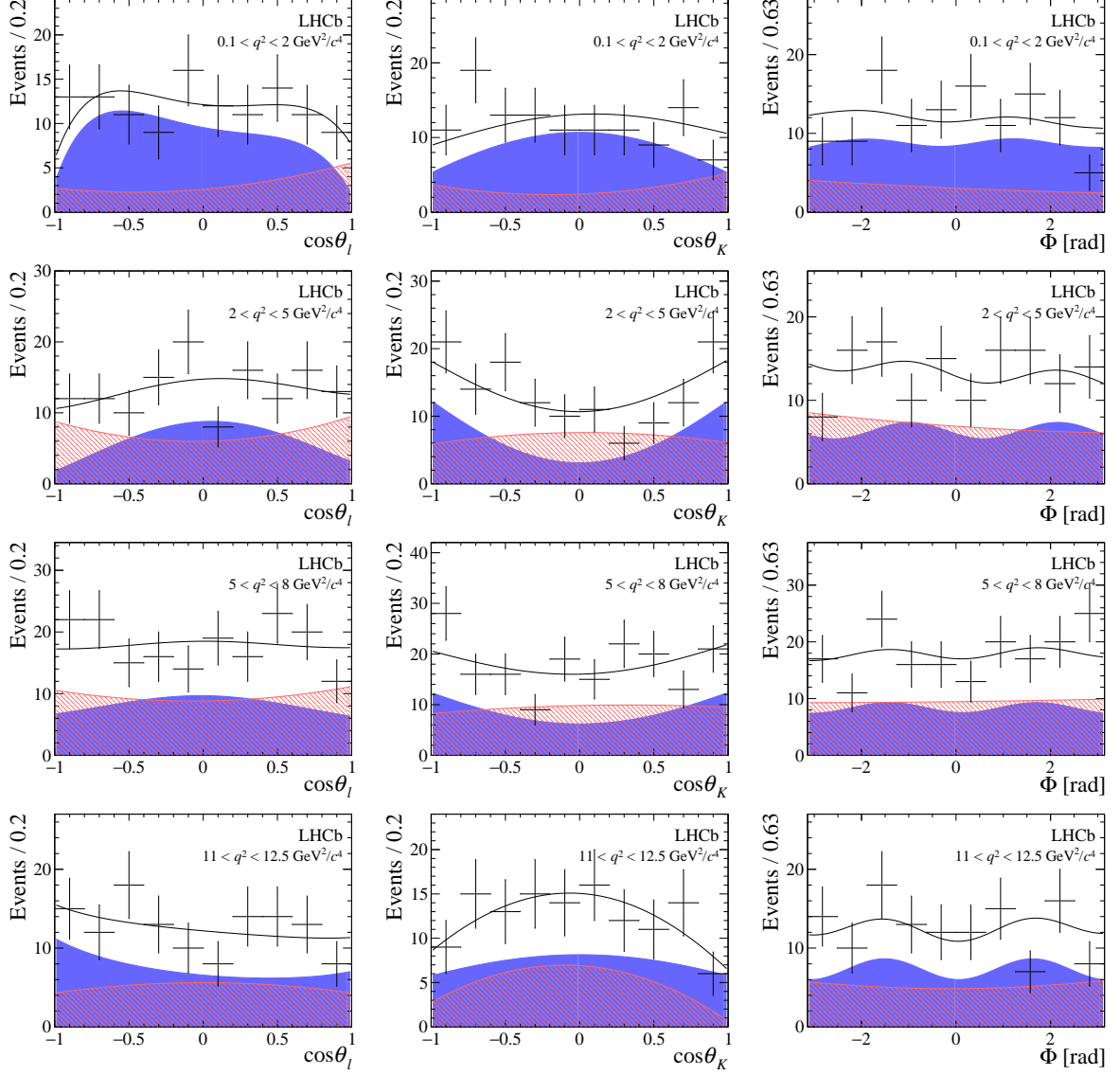


Figure 7: One-dimensional projections of the fit to the angles $\cos\theta_l$, $\cos\theta_K$, Φ in bins of q^2 . The signal component is shown by the solid blue area, the background component by the shaded red area.

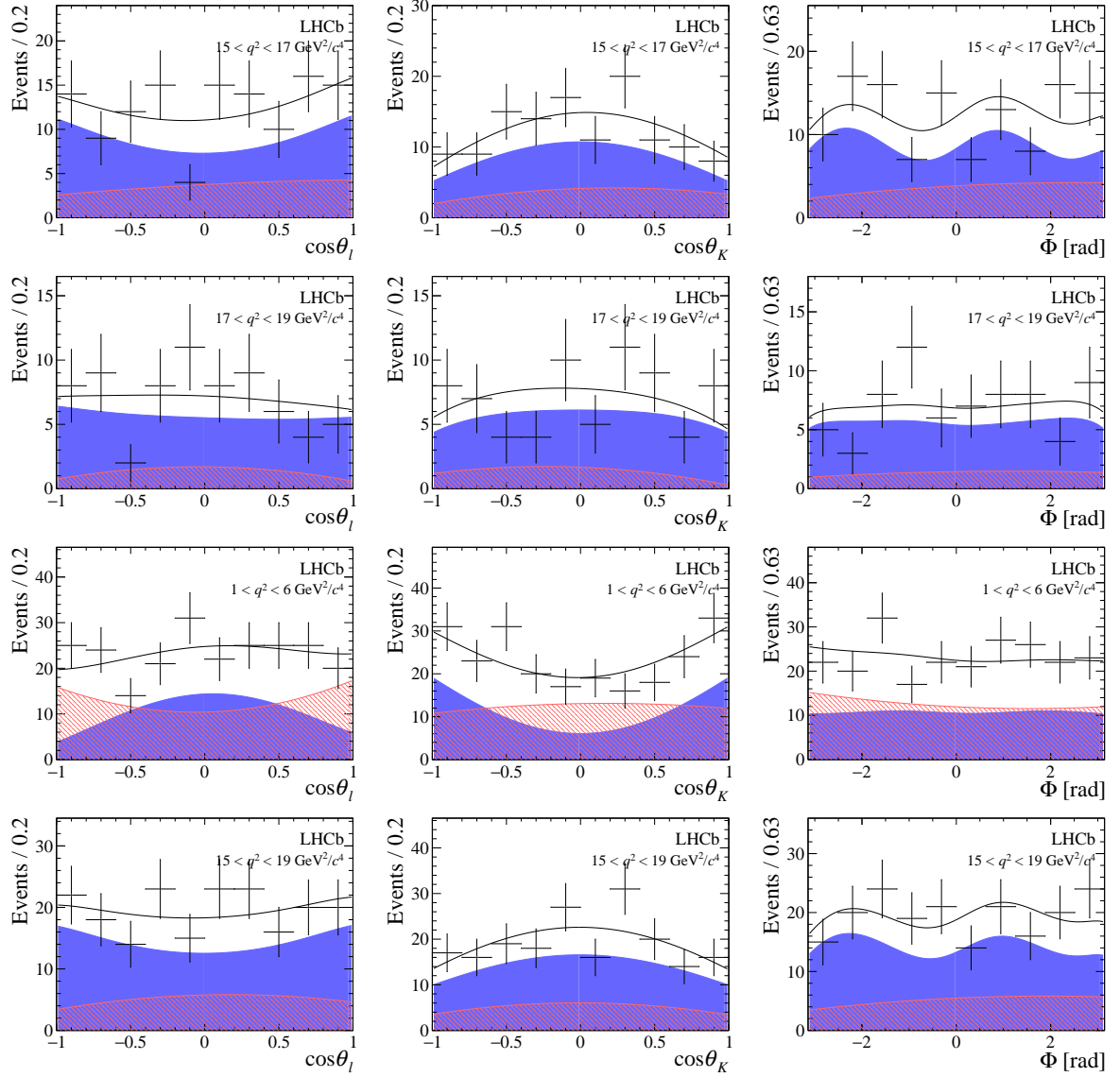


Figure 8: One-dimensional projections of the fit to the angles $\cos\theta_l$, $\cos\theta_K$, Φ in bins of q^2 . The signal component is shown by the solid blue area, the background component by the shaded red area.

C Confidence intervals

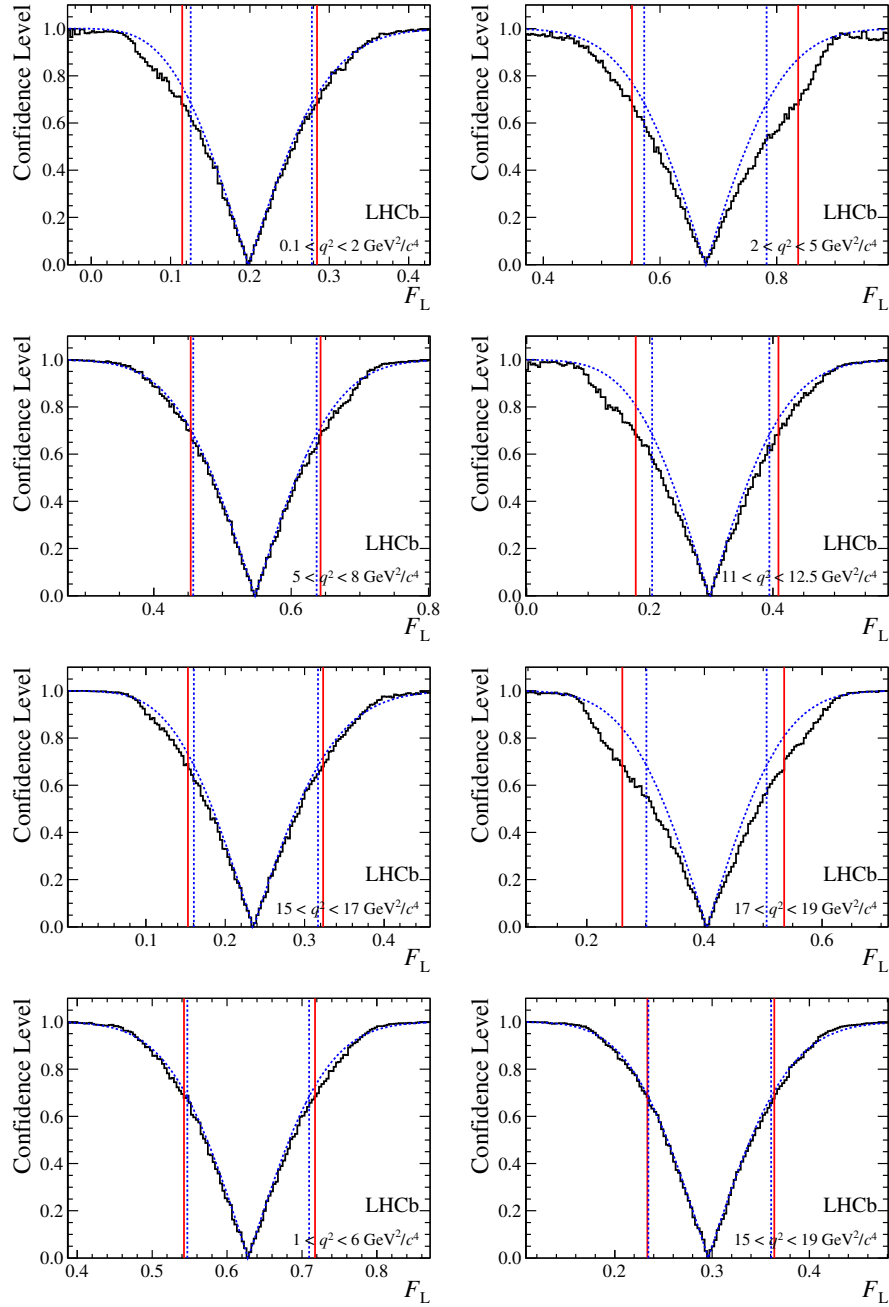


Figure 9: Confidence level obtained from a likelihood scan (shaded blue) and from the Feldman-Cousins method (solid black). The shaded blue and solid red vertical lines indicate the corresponding 68% CL intervals obtained from the likelihood scan and the Feldman-Cousins method, respectively.

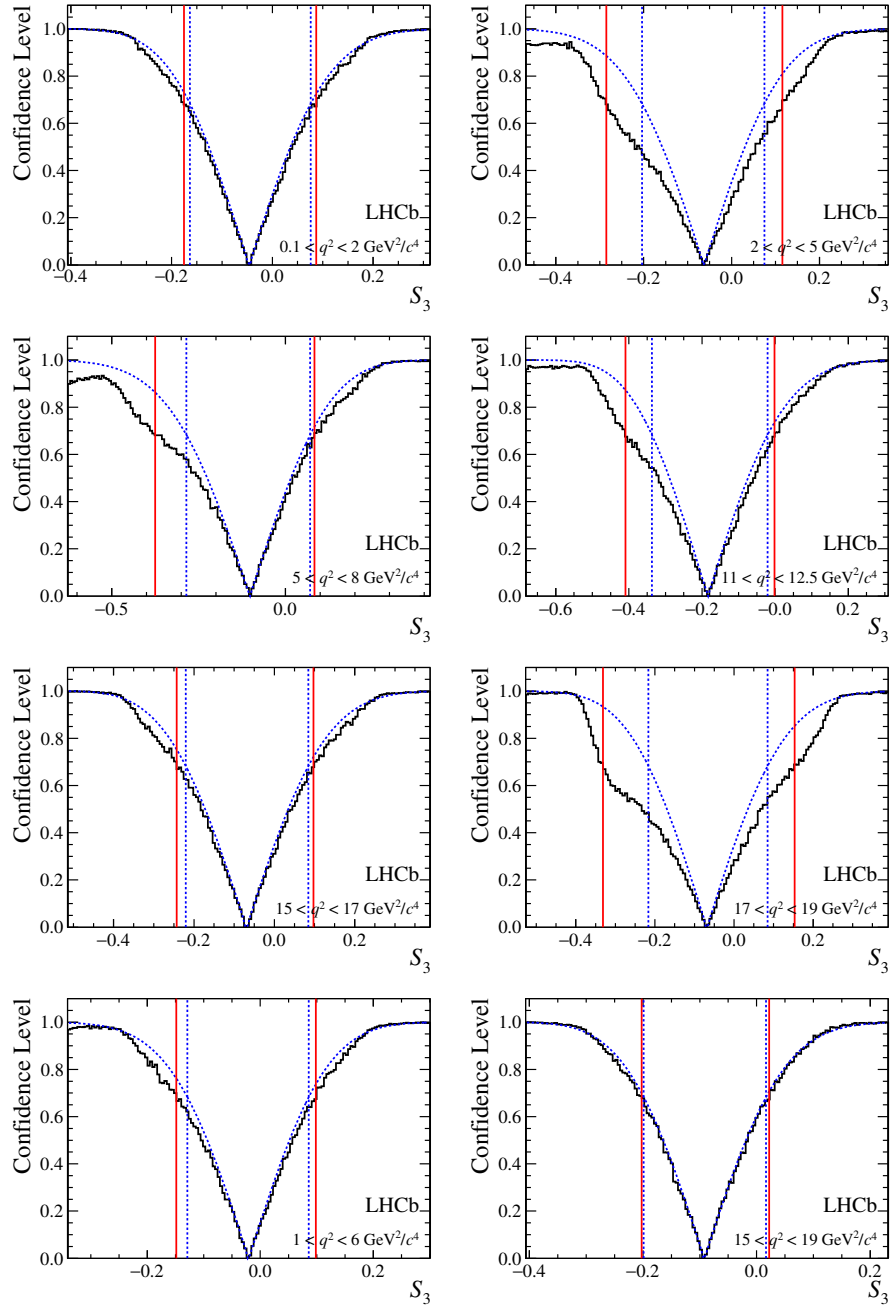


Figure 10: Confidence level obtained from a likelihood scan (shaded blue) and from a Feldman-Cousins method (solid black). The shaded blue and solid red vertical lines indicate the corresponding 68% CL intervals obtained from the likelihood scan and the Feldman-Cousins method, respectively.

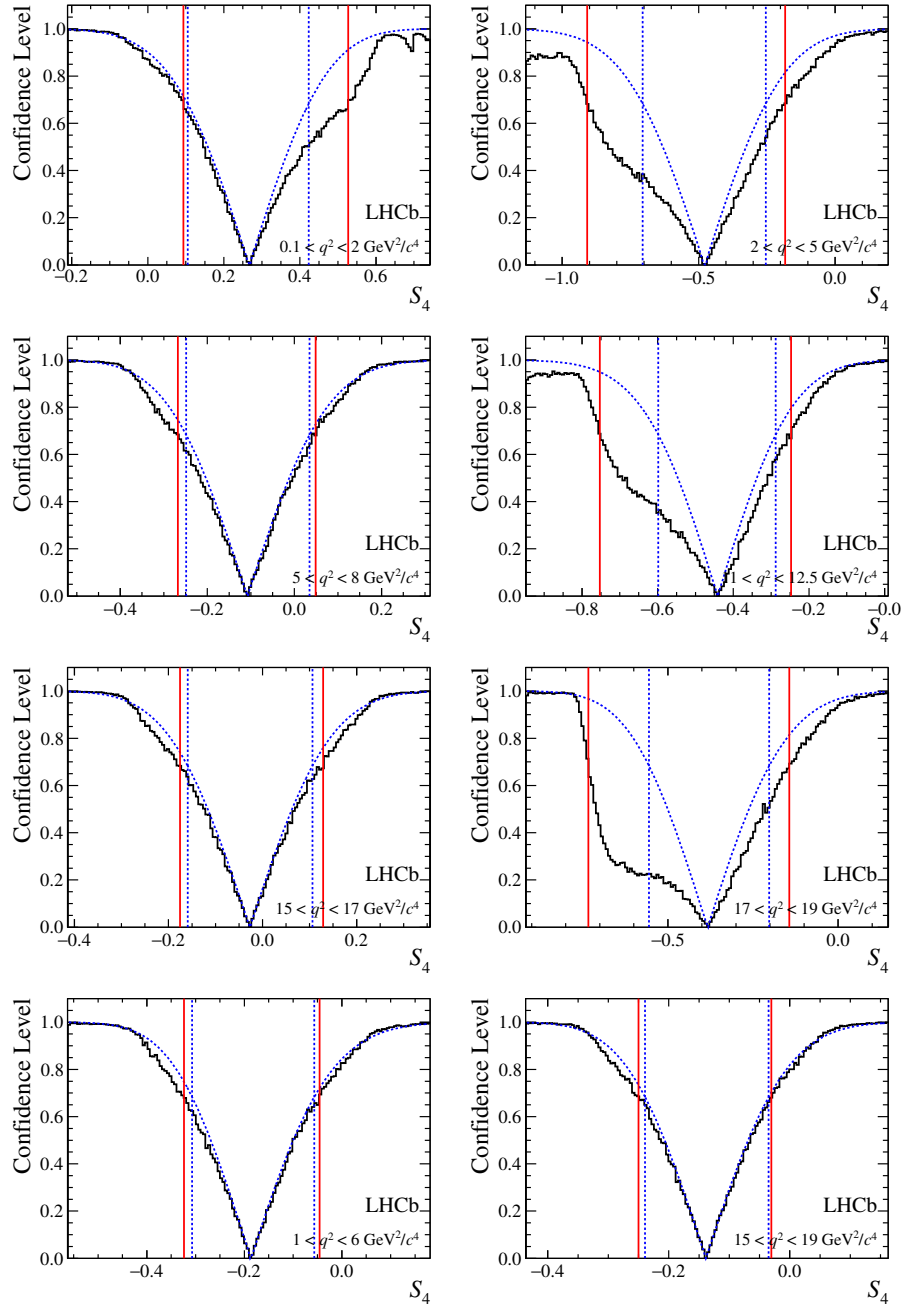


Figure 11: Confidence level obtained from a likelihood scan (shaded blue) and from a Feldman-Cousins method (solid black). The shaded blue and solid red vertical lines indicate the corresponding 68% CL intervals obtained from the likelihood scan and the Feldman-Cousins method, respectively.

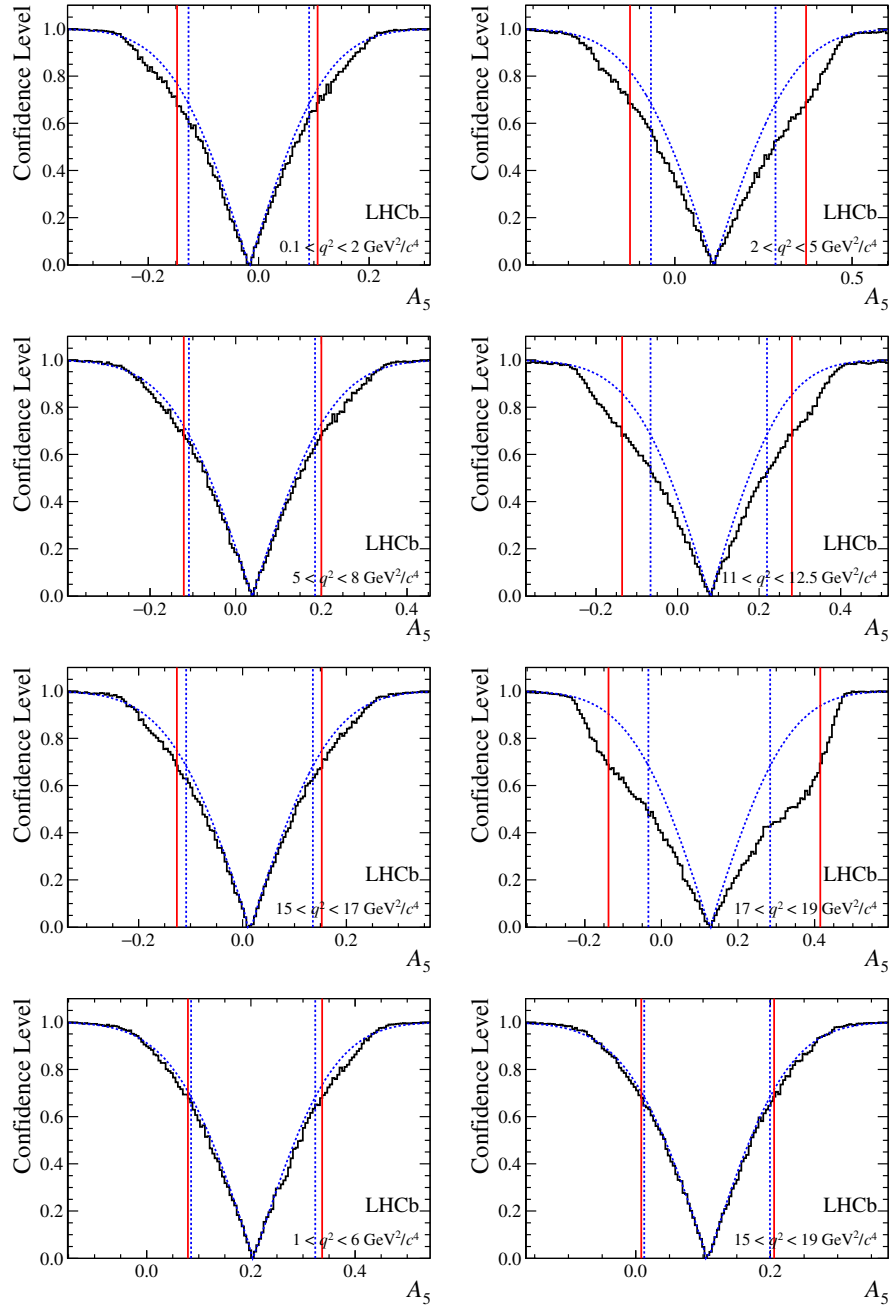


Figure 12: Confidence level obtained from a likelihood scan (shaded blue) and from a Feldman-Cousins method (solid black). The shaded blue and solid red vertical lines indicate the corresponding 68% CL intervals obtained from the likelihood scan and the Feldman-Cousins method, respectively.

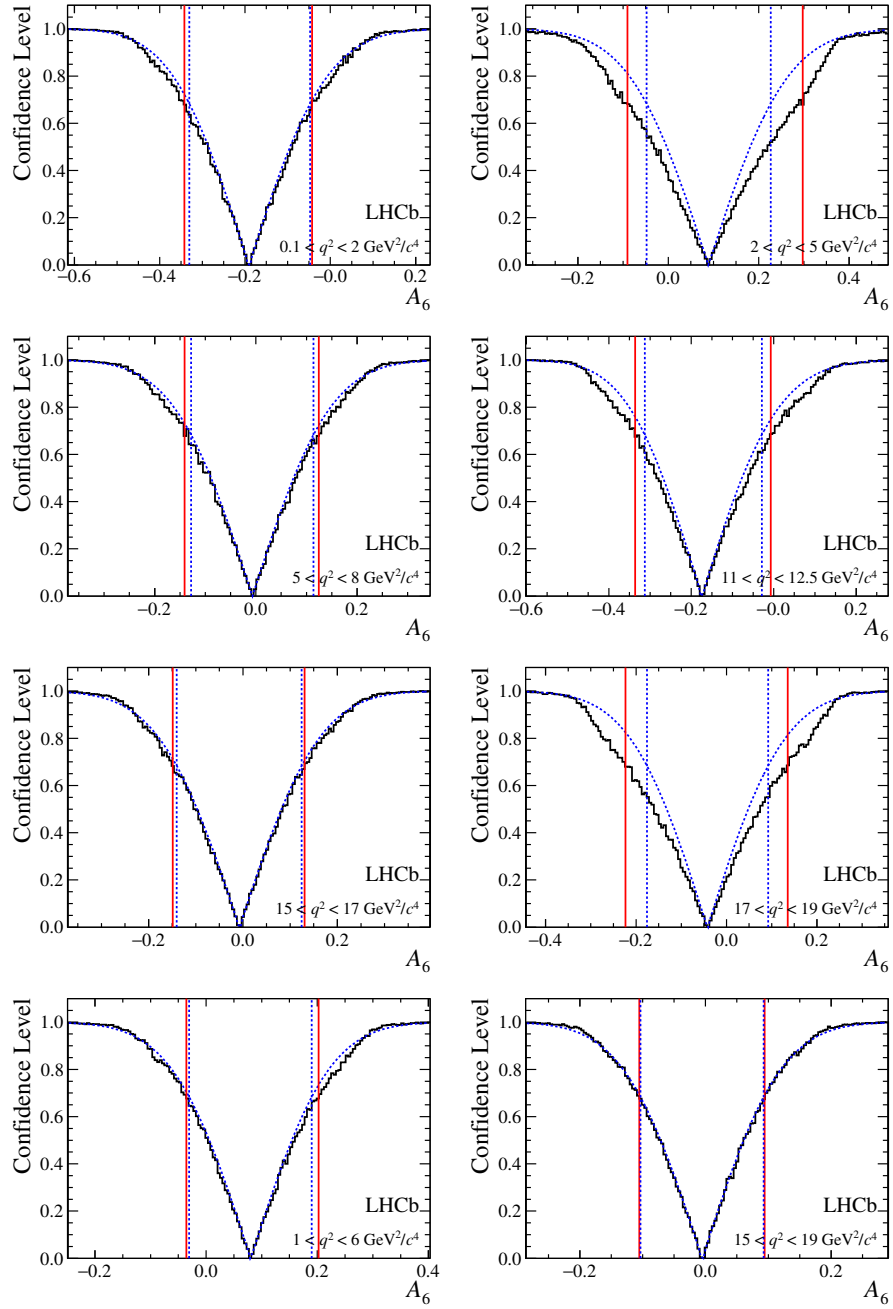


Figure 13: Confidence level obtained from a likelihood scan (shaded blue) and from a Feldman-Cousins method (solid black). The shaded blue and solid red vertical lines indicate the corresponding 68% CL intervals obtained from the likelihood scan and the Feldman-Cousins method, respectively.

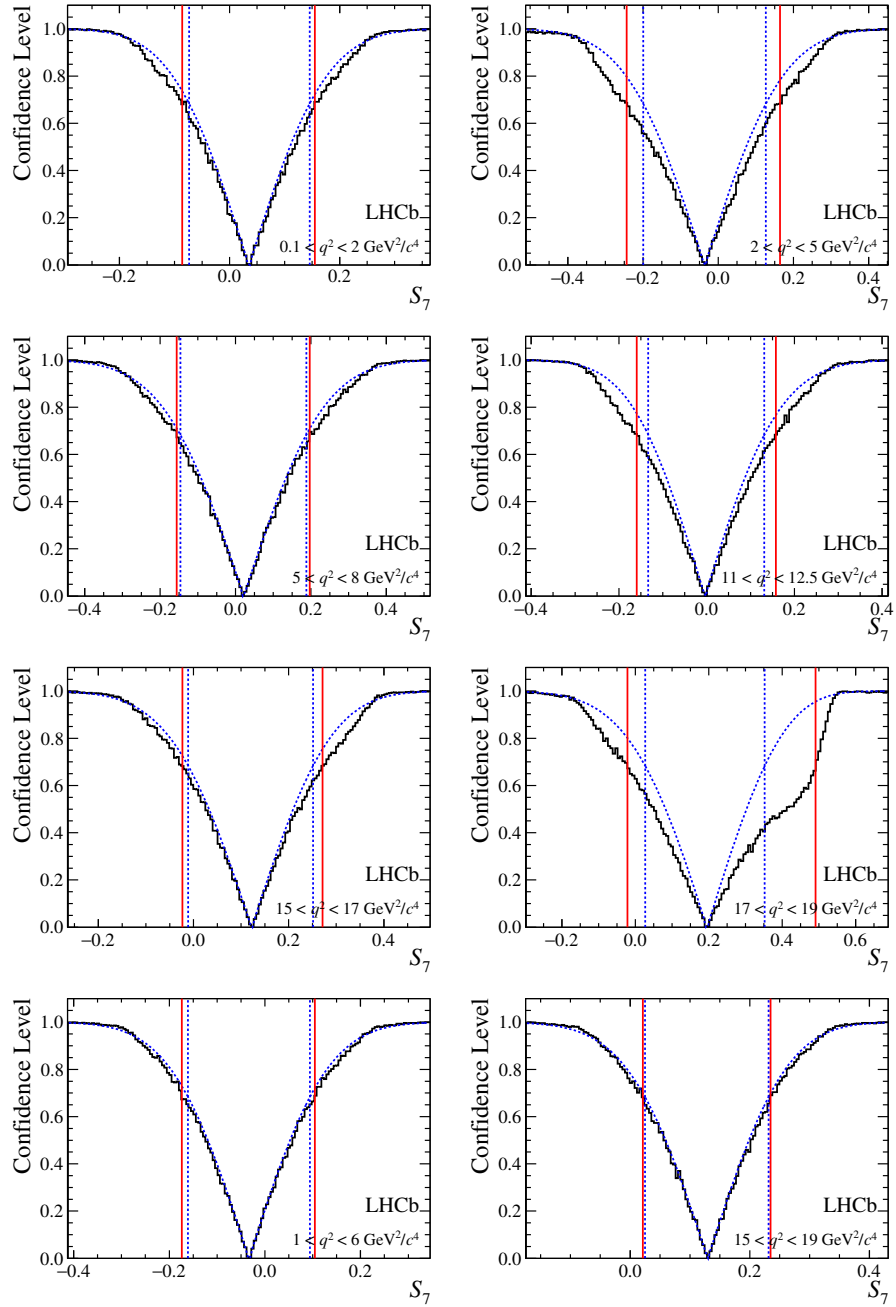


Figure 14: Confidence level obtained from a likelihood scan (shaded blue) and from a Feldman-Cousins method (solid black). The shaded blue and solid red vertical lines indicate the corresponding 68% CL intervals obtained from the likelihood scan and the Feldman-Cousins method, respectively.

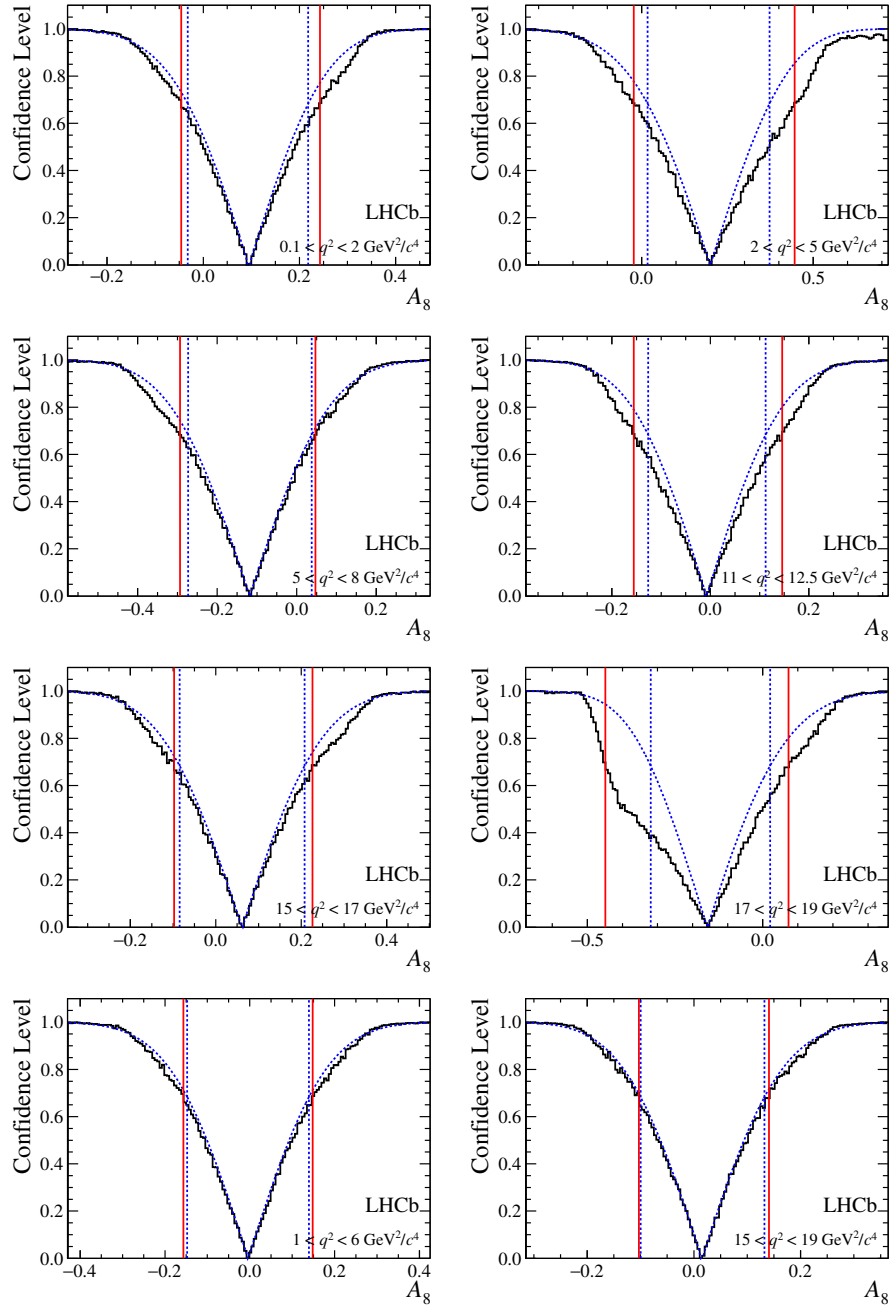


Figure 15: Confidence level obtained from a likelihood scan (shaded blue) and from a Feldman-Cousins method (solid black). The shaded blue and solid red vertical lines indicate the corresponding 68% CL intervals obtained from the likelihood scan and the Feldman-Cousins method, respectively.

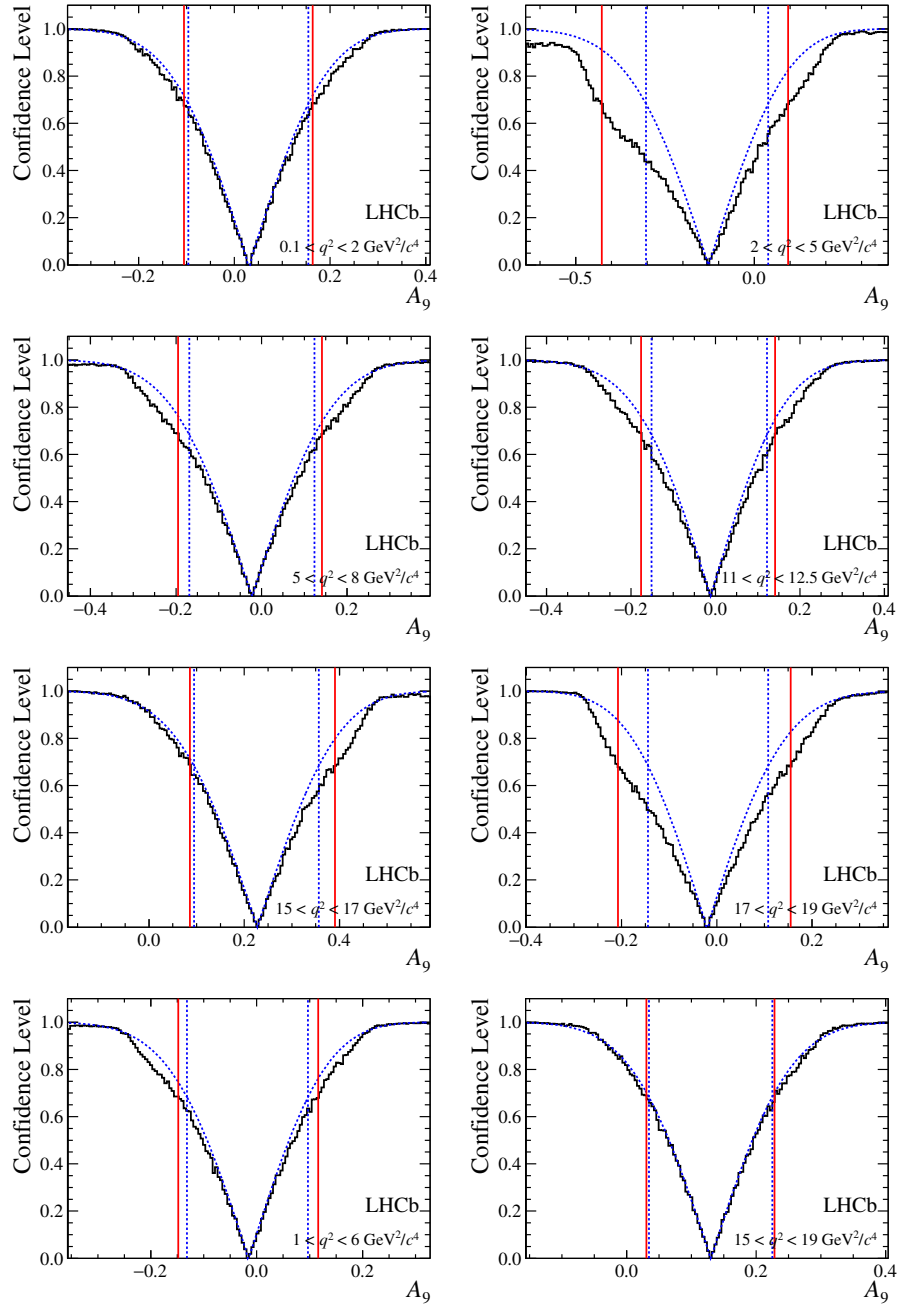


Figure 16: Confidence level obtained from a likelihood scan (shaded blue) and from a Feldman-Cousins method (solid black). The shaded blue and solid red vertical lines indicate the corresponding 68% CL intervals obtained from the likelihood scan and the Feldman-Cousins method, respectively.

D Correlation matrices

Table 4: Correlation matrices for the q^2 bins $0.1 < q^2 < 2.0 \text{ GeV}^2/c^4$, $2.0 < q^2 < 5.0 \text{ GeV}^2/c^4$ and $5.0 < q^2 < 8.0 \text{ GeV}^2/c^4$.

Correlation matrix for $0.1 < q^2 < 2.0 \text{ GeV}^2/c^4$								
	F_L	S_3	S_4	A_5	A_6	S_7	A_8	A_9
F_L	1.00	0.03	-0.15	—	0.02	0.10	0.03	—
S_3		1.00	0.04	0.07	—	0.05	-0.18	-0.05
S_4			1.00	-0.13	-0.09	-0.19	0.06	-0.09
A_5				1.00	0.11	0.06	-0.14	0.10
A_6					1.00	0.07	-0.03	-0.16
S_7						1.00	-0.30	0.03
A_8							1.00	0.06
A_9								1.00

Correlation matrix for $2.0 < q^2 < 5.0 \text{ GeV}^2/c^4$								
	F_L	S_3	S_4	A_5	A_6	S_7	A_8	A_9
F_L	1.00	-0.05	0.27	0.04	-0.09	0.02	0.02	-0.16
S_3		1.00	-0.23	-0.06	-0.05	0.20	-0.11	0.40
S_4			1.00	0.11	0.16	0.14	-0.41	-0.33
A_5				1.00	-0.24	-0.31	0.06	0.08
A_6					1.00	-0.03	0.05	0.11
S_7						1.00	-0.05	-0.02
A_8							1.00	-0.16
A_9								1.00

Correlation matrix for $5.0 < q^2 < 8.0 \text{ GeV}^2/c^4$								
	F_L	S_3	S_4	A_5	A_6	S_7	A_8	A_9
F_L	1.00	-0.03	-0.01	0.11	0.01	0.03	-0.07	0.09
S_3		1.00	-0.03	-0.01	-0.02	-0.18	—	0.05
S_4			1.00	-0.05	-0.01	-0.03	0.20	-0.08
A_5				1.00	—	0.14	-0.05	-0.16
A_6					1.00	—	0.05	-0.25
S_7						1.00	0.04	-0.14
A_8							1.00	-0.04
A_9								1.00

Table 5: Correlation matrices for the q^2 bins $11.0 < q^2 < 12.5 \text{ GeV}^2/c^4$, $15.0 < q^2 < 17.0 \text{ GeV}^2/c^4$ and $17.0 < q^2 < 19.0 \text{ GeV}^2/c^4$.

Correlation matrix for $11.0 < q^2 < 12.5 \text{ GeV}^2/c^4$								
	F_L	S_3	S_4	A_5	A_6	S_7	A_8	A_9
F_L	1.00	0.21	0.11	0.20	0.06	0.21	-0.05	0.03
S_3		1.00	0.02	0.12	0.18	0.08	-0.02	0.04
S_4			1.00	-0.11	-0.37	0.26	-0.01	-0.09
A_5				1.00	-0.16	-0.07	0.22	0.04
A_6					1.00	-0.04	-0.11	0.14
S_7						1.00	-0.36	0.08
A_8							1.00	-0.23
A_9								1.00

Correlation matrix for $15.0 < q^2 < 17.0 \text{ GeV}^2/c^4$								
	F_L	S_3	S_4	A_5	A_6	S_7	A_8	A_9
F_L	1.00	-0.01	-0.01	0.07	-0.05	0.06	-0.06	-0.06
S_3		1.00	0.03	-0.06	0.11	-0.08	-0.06	0.15
S_4			1.00	0.01	-0.07	0.04	0.22	0.04
A_5				1.00	-0.04	0.14	0.05	0.01
A_6					1.00	0.05	0.01	-0.09
S_7						1.00	-0.03	0.06
A_8							1.00	-0.11
A_9								1.00

Correlation matrix for $17.0 < q^2 < 19.0 \text{ GeV}^2/c^4$								
	F_L	S_3	S_4	A_5	A_6	S_7	A_8	A_9
F_L	1.00	-0.12	0.08	-0.32	0.06	-0.04	0.15	-0.01
S_3		1.00	-0.04	0.40	0.16	0.22	—	0.02
S_4			1.00	0.25	0.30	-0.13	0.40	0.14
A_5				1.00	-0.05	0.16	-0.06	0.28
A_6					1.00	-0.03	0.19	-0.05
S_7						1.00	-0.02	0.18
A_8							1.00	-0.02
A_9								1.00

Table 6: Correlation matrices for the q^2 bins $1.0 < q^2 < 6.0 \text{ GeV}^2/c^4$ and $15.0 < q^2 < 19.0 \text{ GeV}^2/c^4$.

Correlation matrix for $1.0 < q^2 < 6.0 \text{ GeV}^2/c^4$								
	F_L	S_3	S_4	A_5	A_6	S_7	A_8	A_9
F_L	1.00	-0.02	0.08	0.08	-0.04	0.07	0.03	-0.05
S_3		1.00	-0.07	0.13	-0.13	0.10	-0.06	0.12
S_4			1.00	0.17	0.10	-0.06	-0.01	-0.13
A_5				1.00	-0.14	-0.05	-0.05	0.04
A_6					1.00	-0.04	-0.09	-0.06
S_7						1.00	0.07	0.04
A_8							1.00	-0.10
A_9								1.00

Correlation matrix for $15.0 < q^2 < 19.0 \text{ GeV}^2/c^4$								
	F_L	S_3	S_4	A_5	A_6	S_7	A_8	A_9
F_L	1.00	0.01	-0.05	-0.03	—	0.07	-0.04	-0.08
S_3		1.00	-0.03	0.16	0.09	0.05	0.02	0.07
S_4			1.00	0.12	0.03	0.03	0.24	0.09
A_5				1.00	-0.09	0.08	0.04	0.14
A_6					1.00	0.05	0.05	-0.11
S_7						1.00	0.01	0.10
A_8							1.00	-0.07
A_9								1.00

References

- [1] CDF collaboration, T. Aaltonen *et al.*, *Measurement of the forward-backward asymmetry in the $B \rightarrow K^{(*)}\mu^+\mu^-$ decay and first observation of the $B_s^0 \rightarrow \phi\mu^+\mu^-$ decay*, Phys. Rev. Lett. **106** (2011) 161801, arXiv:1101.1028.
- [2] CDF collaboration, T. Aaltonen *et al.*, *Observation of the baryonic flavor-changing neutral current decay $\Lambda_b \rightarrow \Lambda\mu^+\mu^-$* , Phys. Rev. Lett. **107** (2011) 201802, arXiv:1107.3753.
- [3] LHCb collaboration, R. Aaij *et al.*, *Differential branching fraction and angular analysis of the decay $B_s^0 \rightarrow \phi\mu^+\mu^-$* , JHEP **07** (2013) 084, arXiv:1305.2168.
- [4] W. Altmannshofer and D. M. Straub, *State of new physics in $b \rightarrow s$ transitions*, arXiv:1411.3161.
- [5] A. Bharucha, D. M. Straub, and R. Zwicky, *$B \rightarrow V\ell^+\ell^-$ in the Standard Model from light-cone sum rules*, arXiv:1503.05534.
- [6] LHCb collaboration, R. Aaij *et al.*, *Differential branching fraction and angular analysis of the decay $B^0 \rightarrow K^{*0}\mu^+\mu^-$* , JHEP **08** (2013) 131, arXiv:1304.6325.
- [7] LHCb collaboration, R. Aaij *et al.*, *Differential branching fractions and isospin asymmetries of $B \rightarrow K^{(*)}\mu^+\mu^-$ decays*, JHEP **06** (2014) 133, arXiv:1403.8044.
- [8] LHCb collaboration, R. Aaij *et al.*, *First observations of the rare decays $B^+ \rightarrow K^+\pi^+\pi^-\mu^+\mu^-$ and $B^+ \rightarrow \phi K^+\mu^+\mu^-$* , JHEP **10** (2014) 064, arXiv:1408.1137.
- [9] LHCb collaboration, R. Aaij *et al.*, *Measurement of form-factor-independent observables in the decay $B^0 \rightarrow K^{*0}\mu^+\mu^-$* , Phys. Rev. Lett. **111** (2013) 191801, arXiv:1308.1707.
- [10] LHCb collaboration, *Angular analysis of the $B^0 \rightarrow K^{*0}\mu^+\mu^-$ decay*, LHCb-CONF-2015-002.
- [11] LHCb collaboration, R. Aaij *et al.*, *Amplitude analysis and branching fraction measurement of $\bar{B}_s^0 \rightarrow J/\psi K^+K^-$* , Phys. Rev. **D87** (2013) 072004, arXiv:1302.1213.
- [12] C. Bobeth, G. Hiller, and G. Piranishvili, *CP asymmetries in $\bar{B} \rightarrow \bar{K}^*(\rightarrow \bar{K}\pi)\bar{\ell}\ell$ and untagged $\bar{B}_s, B_s \rightarrow \phi(\rightarrow K^+K^-)\bar{\ell}\ell$ decays at NLO*, JHEP **07** (2008) 106, arXiv:0805.2525.
- [13] LHCb collaboration, A. A. Alves Jr. *et al.*, *The LHCb detector at the LHC*, JINST **3** (2008) S08005.
- [14] LHCb collaboration, R. Aaij *et al.*, *LHCb detector performance*, Int. J. Mod. Phys. **A30** (2015) 1530022, arXiv:1412.6352.

- [15] R. Aaij *et al.*, *The LHCb trigger and its performance in 2011*, JINST **8** (2013) P04022, arXiv:1211.3055.
- [16] T. Sjöstrand, S. Mrenna, and P. Skands, *PYTHIA 6.4 physics and manual*, JHEP **05** (2006) 026, arXiv:hep-ph/0603175; T. Sjöstrand, S. Mrenna, and P. Skands, *A brief introduction to PYTHIA 8.1*, Comput. Phys. Commun. **178** (2008) 852, arXiv:0710.3820.
- [17] I. Belyaev *et al.*, *Handling of the generation of primary events in Gauss, the LHCb simulation framework*, J. Phys. Conf. Ser. **331** (2011) 032047.
- [18] D. J. Lange, *The EvtGen particle decay simulation package*, Nucl. Instrum. Meth. **A462** (2001) 152.
- [19] P. Golonka and Z. Was, *PHOTOS Monte Carlo: A precision tool for QED corrections in Z and W decays*, Eur. Phys. J. **C45** (2006) 97, arXiv:hep-ph/0506026.
- [20] Geant4 collaboration, J. Allison *et al.*, *Geant4 developments and applications*, IEEE Trans. Nucl. Sci. **53** (2006) 270; Geant4 collaboration, S. Agostinelli *et al.*, *Geant4: a simulation toolkit*, Nucl. Instrum. Meth. **A506** (2003) 250.
- [21] M. Clemencic *et al.*, *The LHCb simulation application, Gauss: design, evolution and experience*, J. Phys. Conf. Ser. **331** (2011) 032023.
- [22] Particle Data Group, K. A. Olive *et al.*, *Review of particle physics*, Chin. Phys. **C38** (2014) 090001.
- [23] L. Breiman, J. H. Friedman, R. A. Olshen, and C. J. Stone, *Classification and regression trees*, Wadsworth international group, Belmont, California, USA, 1984.
- [24] R. E. Schapire and Y. Freund, *A decision-theoretic generalization of on-line learning and an application to boosting*, J. Comput. Syst. Sci. **55** (1997) 119.
- [25] L. Mott and W. Roberts, *Rare dileptonic decays of Λ_b in a quark model*, Int. J. Mod. Phys. **A27** (2012) 1250016, arXiv:1108.6129.
- [26] LHCb collaboration, R. Aaij *et al.*, *Measurement of the differential branching fraction of the decay $\Lambda_b^0 \rightarrow \Lambda \mu^+ \mu^-$* , Phys. Lett. **B725** (2013) 25, arXiv:1306.2577.
- [27] LHCb collaboration, R. Aaij *et al.*, *Measurement of the fragmentation fraction ratio f_s/f_d and its dependence on B meson kinematics*, JHEP **04** (2013) 001, arXiv:1301.5286, f_s/f_d value updated in LHCb-CONF-2013-011.
- [28] Belle collaboration, F. Thorne *et al.*, *Measurement of the decays $B_s^0 \rightarrow J/\psi \phi(1020)$, $B_s^0 \rightarrow J/\psi f_2(1525)$ and $B_s^0 \rightarrow J/\psi K^+ K^-$ at Belle*, Phys. Rev. **D88** (2013) 114006, arXiv:1309.0704.

- [29] CDF collaboration, F. Abe *et al.*, *Ratios of bottom meson branching fractions involving J/ψ mesons and determination of b quark fragmentation fractions*, Phys. Rev. **D54** (1996) 6596, [arXiv:hep-ex/9607003](#).
- [30] R. R. Horgan, Z. Liu, S. Meinel, and M. Wingate, *Lattice QCD calculation of form factors describing the rare decays $B \rightarrow K^* \ell^+ \ell^-$ and $B_s \rightarrow \phi \ell^+ \ell^-$* , Phys. Rev. **D89** (2014) 094501, [arXiv:1310.3722](#).
- [31] R. R. Horgan, Z. Liu, S. Meinel, and M. Wingate, *Rare B decays using lattice QCD form factors*, PoS(LATTICE2014)372 (2015) [arXiv:1501.00367](#).
- [32] A. Ali, E. Lunghi, C. Greub, and G. Hiller, *Improved model independent analysis of semileptonic and radiative rare B decays*, Phys. Rev. **D66** (2002) 034002, [arXiv:hep-ph/0112300](#).
- [33] P. Ball and R. Zwicky, *$B_{d,s} \rightarrow \rho, \omega, K^*, \phi$ decay form factors from light-cone sum rules reexamined*, Phys. Rev. **D71** (2005) 014029, [arXiv:hep-ph/0412079](#).
- [34] LHCb collaboration, R. Aaij *et al.*, *Precision measurement of CP violation in $B_s^0 \rightarrow J/\psi K^+ K^-$ decays*, Phys. Rev. Lett. **114** (2015) 041801, [arXiv:1411.3104](#).
- [35] K. De Bruyn *et al.*, *Branching ratio measurements of B_s decays*, Phys. Rev. **D86** (2012) 014027, [arXiv:1204.1735](#).
- [36] G. J. Feldman and R. D. Cousins, *A unified approach to the classical statistical analysis of small signals*, Phys. Rev. **D57** (1998) 3873, [arXiv:physics/9711021](#).
- [37] B. Sen, M. Walker, and M. Woodroffe, *On the unified method with nuisance parameters*, Statist. Sinica **19** (2009) 301.

LHCb collaboration

R. Aaij³⁸, B. Adeva³⁷, M. Adinolfi⁴⁶, A. Affolder⁵², Z. Ajaltouni⁵, S. Akar⁶, J. Albrecht⁹, F. Alessio³⁸, M. Alexander⁵¹, S. Ali⁴¹, G. Alkhazov³⁰, P. Alvarez Cartelle⁵³, A.A. Alves Jr⁵⁷, S. Amato², S. Amerio²², Y. Amhis⁷, L. An³, L. Anderlini^{17,g}, J. Anderson⁴⁰, G. Andreassi³⁹, M. Andreotti^{16,f}, J.E. Andrews⁵⁸, R.B. Appleby⁵⁴, O. Aquines Gutierrez¹⁰, F. Archilli³⁸, P. d'Argent¹¹, A. Artamonov³⁵, M. Artuso⁵⁹, E. Aslanides⁶, G. Auriemma^{25,n}, M. Baalouch⁵, S. Bachmann¹¹, J.J. Back⁴⁸, A. Badalov³⁶, C. Baesso⁶⁰, W. Baldini^{16,38}, R.J. Barlow⁵⁴, C. Barschel³⁸, S. Barsuk⁷, W. Barter³⁸, V. Batozskaya²⁸, V. Battista³⁹, A. Bay³⁹, L. Beaucourt⁴, J. Beddow⁵¹, F. Bedeschi²³, I. Bediaga¹, L.J. Bel⁴¹, V. Bellec³⁹, I. Belyaev³¹, E. Ben-Haim⁸, G. Bencivenni¹⁸, S. Benson³⁸, J. Benton⁴⁶, A. Berezhnoy³², R. Bernet⁴⁰, A. Bertolin²², M.-O. Bettler³⁸, M. van Beuzekom⁴¹, A. Bien¹¹, S. Bifani⁴⁵, T. Bird⁵⁴, A. Birnkraut⁹, A. Bizzeti^{17,i}, T. Blake⁴⁸, F. Blanc³⁹, J. Blouw¹⁰, S. Blusk⁵⁹, V. Bocci²⁵, A. Bondar³⁴, N. Bondar^{30,38}, W. Bonivento¹⁵, S. Borghi⁵⁴, M. Borsato⁷, T.J.V. Bowcock⁵², E. Bowen⁴⁰, C. Bozzi¹⁶, S. Braun¹¹, D. Brett⁵⁴, M. Britsch¹⁰, T. Britton⁵⁹, J. Brodzicka⁵⁴, N.H. Brook⁴⁶, A. Bursche⁴⁰, J. Buytaert³⁸, S. Cadeddu¹⁵, R. Calabrese^{16,f}, M. Calvi^{20,k}, M. Calvo Gomez^{36,p}, P. Campana¹⁸, D. Campora Perez³⁸, L. Capriotti⁵⁴, A. Carbone^{14,d}, G. Carboni^{24,l}, R. Cardinale^{19,j}, A. Cardini¹⁵, P. Carniti²⁰, L. Carson⁵⁰, K. Carvalho Akiba^{2,38}, G. Casse⁵², L. Cassina^{20,k}, L. Castillo Garcia³⁸, M. Cattaneo³⁸, Ch. Cauet⁹, G. Cavallero¹⁹, R. Cenci^{23,t}, M. Charles⁸, Ph. Charpentier³⁸, M. Chefdeville⁴, S. Chen⁵⁴, S.-F. Cheung⁵⁵, N. Chiapolini⁴⁰, M. Chrzaszcz⁴⁰, X. Cid Vidal³⁸, G. Ciezarek⁴¹, P.E.L. Clarke⁵⁰, M. Clemencic³⁸, H.V. Cliff⁴⁷, J. Closier³⁸, V. Coco³⁸, J. Cogan⁶, E. Cogneras⁵, V. Cogoni^{15,e}, L. Cojocariu²⁹, G. Collazuol²², P. Collins³⁸, A. Comerma-Montells¹¹, A. Contu^{15,38}, A. Cook⁴⁶, M. Coombes⁴⁶, S. Coquereau⁸, G. Corti³⁸, M. Corvo^{16,f}, B. Couturier³⁸, G.A. Cowan⁵⁰, D.C. Craik⁴⁸, A. Crocombe⁴⁸, M. Cruz Torres⁶⁰, S. Cunliffe⁵³, R. Currie⁵³, C. D'Ambrosio³⁸, E. Dall'Occo⁴¹, J. Dalseno⁴⁶, P.N.Y. David⁴¹, A. Davis⁵⁷, K. De Bruyn⁴¹, S. De Capua⁵⁴, M. De Cian¹¹, J.M. De Miranda¹, L. De Paula², P. De Simone¹⁸, C.-T. Dean⁵¹, D. Decamp⁴, M. Deckenhoff⁹, L. Del Buono⁸, N. Déleage⁴, M. Demmer⁹, D. Derkach⁵⁵, O. Deschamps⁵, F. Dettori³⁸, B. Dey²¹, A. Di Canto³⁸, F. Di Ruscio²⁴, H. Dijkstra³⁸, S. Donleavy⁵², F. Dordei¹¹, M. Dorigo³⁹, A. Dosil Suárez³⁷, D. Dossett⁴⁸, A. Dovbnya⁴³, K. Dreimanis⁵², L. Dufour⁴¹, G. Dujany⁵⁴, F. Dupertuis³⁹, P. Durante³⁸, R. Dzhelyadin³⁵, A. Dziurda²⁶, A. Dzyuba³⁰, S. Easo^{49,38}, U. Egede⁵³, V. Egorychev³¹, S. Eidelman³⁴, S. Eisenhardt⁵⁰, U. Eitschberger⁹, R. Ekelhof⁹, L. Eklund⁵¹, I. El Rifai⁵, Ch. Elsasser⁴⁰, S. Ely⁵⁹, S. Esen¹¹, H.M. Evans⁴⁷, T. Evans⁵⁵, A. Falabella¹⁴, C. Färber³⁸, C. Farinelli⁴¹, N. Farley⁴⁵, S. Farry⁵², R. Fay⁵², D. Ferguson⁵⁰, V. Fernandez Albor³⁷, F. Ferrari¹⁴, F. Ferreira Rodrigues¹, M. Ferro-Luzzi³⁸, S. Filippov³³, M. Fiore^{16,38,f}, M. Fiorini^{16,f}, M. Firlej²⁷, C. Fitzpatrick³⁹, T. Fiutowski²⁷, K. Fohl³⁸, P. Fol⁵³, M. Fontana¹⁰, F. Fontanelli^{19,j}, R. Forty³⁸, O. Francisco², M. Frank³⁸, C. Frei³⁸, M. Frosini¹⁷, J. Fu²¹, E. Furfaro^{24,l}, A. Gallas Torreira³⁷, D. Galli^{14,d}, S. Gallorini^{22,38}, S. Gambetta⁵⁰, M. Gandelman², P. Gandini⁵⁵, Y. Gao³, J. García Pardiñas³⁷, J. Garra Tico⁴⁷, L. Garrido³⁶, D. Gascon³⁶, C. Gaspar³⁸, R. Gauld⁵⁵, L. Gavardi⁹, G. Gazzoni⁵, A. Geraci^{21,v}, D. Gerick¹¹, E. Gersabeck¹¹, M. Gersabeck⁵⁴, T. Gershon⁴⁸, Ph. Ghez⁴, A. Gianelle²², S. Giani³⁹, V. Gibson⁴⁷, O. G. Girard³⁹, L. Giubega²⁹, V.V. Gligorov³⁸, C. Göbel⁶⁰, D. Golubkov³¹, A. Golutvin^{53,31,38}, A. Gomes^{1,a}, C. Gotti^{20,k}, M. Grabalosa Gándara⁵, R. Graciani Diaz³⁶, L.A. Granado Cardoso³⁸, E. Graugés³⁶, E. Graverini⁴⁰, G. Graziani¹⁷, A. Grecu²⁹, E. Greening⁵⁵, S. Gregson⁴⁷, P. Griffith⁴⁵, L. Grillo¹¹, O. Grünberg⁶³, B. Gui⁵⁹, E. Gushchin³³, Yu. Guz^{35,38}, T. Gys³⁸, T. Hadavizadeh⁵⁵, C. Hadjivasiliou⁵⁹, G. Haefeli³⁹, C. Haen³⁸,

S.C. Haines⁴⁷, S. Hall⁵³, B. Hamilton⁵⁸, X. Han¹¹, S. Hansmann-Menzemer¹¹, N. Harnew⁵⁵,
 S.T. Harnew⁴⁶, J. Harrison⁵⁴, J. He³⁸, T. Head³⁹, V. Heijne⁴¹, K. Hennessy⁵², P. Henrard⁵,
 L. Henry⁸, J.A. Hernando Morata³⁷, E. van Herwijnen³⁸, M. Heß⁶³, A. Hicheur², D. Hill⁵⁵,
 M. Hoballah⁵, C. Hombach⁵⁴, W. Hulsbergen⁴¹, T. Humair⁵³, N. Hussain⁵⁵, D. Hutchcroft⁵²,
 D. Hynds⁵¹, M. Idzik²⁷, P. Ilten⁵⁶, R. Jacobsson³⁸, A. Jaeger¹¹, J. Jalocha⁵⁵, E. Jans⁴¹,
 A. Jawahery⁵⁸, F. Jing³, M. John⁵⁵, D. Johnson³⁸, C.R. Jones⁴⁷, C. Joram³⁸, B. Jost³⁸,
 N. Jurik⁵⁹, S. Kandybei⁴³, W. Kanso⁶, M. Karacson³⁸, T.M. Karbach^{38,†}, S. Karodia⁵¹,
 M. Kelsey⁵⁹, I.R. Kenyon⁴⁵, M. Kenzie³⁸, T. Ketel⁴², B. Khanji^{20,38,k}, C. Khurewathanakul³⁹,
 S. Klaver⁵⁴, K. Klimaszewski²⁸, O. Kochebina⁷, M. Kolpin¹¹, I. Komarov³⁹, R.F. Koopman⁴²,
 P. Koppenburg^{41,38}, M. Kozeiha⁵, L. Kravchuk³³, K. Kreplin¹¹, M. Krepis⁴⁸, G. Krocker¹¹,
 P. Krokovny³⁴, F. Kruse⁹, W. Kucewicz^{26,o}, M. Kucharczyk²⁶, V. Kudryavtsev³⁴, A.
 K. Kuonen³⁹, K. Kurek²⁸, T. Kvaratskheliya³¹, D. Lacarrere³⁸, G. Lafferty⁵⁴, A. Lai¹⁵,
 D. Lambert⁵⁰, G. Lanfranchi¹⁸, C. Langenbruch⁴⁸, B. Langhans³⁸, T. Latham⁴⁸, C. Lazzeroni⁴⁵,
 R. Le Gac⁶, J. van Leerdam⁴¹, J.-P. Lees⁴, R. Lefèvre⁵, A. Leflat^{32,38}, J. Lefrançois⁷, O. Leroy⁶,
 T. Lesiak²⁶, B. Leverington¹¹, Y. Li⁷, T. Likhomanenko^{65,64}, M. Liles⁵², R. Lindner³⁸, C. Linn³⁸,
 F. Lionetto⁴⁰, B. Liu¹⁵, X. Liu³, D. Loh⁴⁸, S. Lohn³⁸, I. Longstaff⁵¹, J.H. Lopes²,
 D. Lucchesi^{22,r}, M. Lucio Martinez³⁷, H. Luo⁵⁰, A. Lupato²², E. Luppi^{16,f}, O. Lupton⁵⁵,
 N. Lusardi²¹, F. Machefert⁷, F. Maciuc²⁹, O. Maev³⁰, K. Maguire⁵⁴, S. Malde⁵⁵, A. Malinin⁶⁴,
 G. Manca⁷, G. Mancinelli⁶, P. Manning⁵⁹, A. Mapelli³⁸, J. Maratas⁵, J.F. Marchand⁴,
 U. Marconi¹⁴, C. Marin Benito³⁶, P. Marino^{23,38,t}, R. Märki³⁹, J. Marks¹¹, G. Martellotti²⁵,
 M. Martin⁶, M. Martinelli³⁹, D. Martinez Santos³⁷, F. Martinez Vidal⁶⁶, D. Martins Tostes²,
 A. Massafferri¹, R. Matev³⁸, A. Mathad⁴⁸, Z. Mathe³⁸, C. Matteuzzi²⁰, K. Matthieu¹¹,
 A. Mauri⁴⁰, B. Maurin³⁹, A. Mazurov⁴⁵, M. McCann⁵³, J. McCarthy⁴⁵, A. McNab⁵⁴,
 R. McNulty¹², B. Meadows⁵⁷, F. Meier⁹, M. Meissner¹¹, D. Melnychuk²⁸, M. Merk⁴¹,
 D.A. Milanes⁶², M.-N. Minard⁴, D.S. Mitzel¹¹, J. Molina Rodriguez⁶⁰, I.A. Monroy⁶²,
 S. Monteil⁵, M. Morandin²², P. Morawski²⁷, A. Mordà⁶, M.J. Morello^{23,t}, J. Moron²⁷,
 A.B. Morris⁵⁰, R. Mountain⁵⁹, F. Muheim⁵⁰, J. Müller⁹, K. Müller⁴⁰, V. Müller⁹, M. Mussini¹⁴,
 B. Muster³⁹, P. Naik⁴⁶, T. Nakada³⁹, R. Nandakumar⁴⁹, A. Nandi⁵⁵, I. Nasteva²,
 M. Needham⁵⁰, N. Neri²¹, S. Neubert¹¹, N. Neufeld³⁸, M. Neuner¹¹, A.D. Nguyen³⁹,
 T.D. Nguyen³⁹, C. Nguyen-Mau^{39,q}, V. Niess⁵, R. Niet⁹, N. Nikitin³², T. Nikodem¹¹, D. Ninci²³,
 A. Novoselov³⁵, D.P. O’Hanlon⁴⁸, A. Oblakowska-Mucha²⁷, V. Obraztsov³⁵, S. Ogilvy⁵¹,
 O. Okhrimenko⁴⁴, R. Oldeman^{15,e}, C.J.G. Onderwater⁶⁷, B. Osorio Rodrigues¹,
 J.M. Otalora Goicochea², A. Otto³⁸, P. Owen⁵³, A. Oyanguren⁶⁶, A. Palano^{13,c}, F. Palombo^{21,u},
 M. Palutan¹⁸, J. Panman³⁸, A. Papanestis⁴⁹, M. Pappagallo⁵¹, L.L. Pappalardo^{16,f},
 C. Pappenheimer⁵⁷, C. Parkes⁵⁴, G. Passaleva¹⁷, G.D. Patel⁵², M. Patel⁵³, C. Patrignani^{19,j},
 A. Pearce^{54,49}, A. Pellegrino⁴¹, G. Penso^{25,m}, M. Pepe Altarelli³⁸, S. Perazzini^{14,d}, P. Perret⁵,
 L. Pescatore⁴⁵, K. Petridis⁴⁶, A. Petrolini^{19,j}, M. Petruzzo²¹, E. Picatoste Olloqui³⁶,
 B. Pietrzyk⁴, T. Pilar⁴⁸, D. Pinci²⁵, A. Pistone¹⁹, A. Piucci¹¹, S. Playfer⁵⁰, M. Plo Casasus³⁷,
 T. Poikela³⁸, F. Polci⁸, A. Poluektov^{48,34}, I. Polyakov³¹, E. Polycarpo², A. Popov³⁵,
 D. Popov^{10,38}, B. Popovici²⁹, C. Potterat², E. Price⁴⁶, J.D. Price⁵², J. Prisciandaro³⁹,
 A. Pritchard⁵², C. Prouve⁴⁶, V. Pugatch⁴⁴, A. Puig Navarro³⁹, G. Punzi^{23,s}, W. Qian⁴,
 R. Quagliani^{7,46}, B. Rachwal²⁶, J.H. Rademacker⁴⁶, M. Rama²³, M.S. Rangel², I. Raniuk⁴³,
 N. Rauschmayr³⁸, G. Raven⁴², F. Redi⁵³, S. Reichert⁵⁴, M.M. Reid⁴⁸, A.C. dos Reis¹,
 S. Ricciardi⁴⁹, S. Richards⁴⁶, M. Rihl³⁸, K. Rinnert⁵², V. Rives Molina³⁶, P. Robbe^{7,38},
 A.B. Rodrigues¹, E. Rodrigues⁵⁴, J.A. Rodriguez Lopez⁶², P. Rodriguez Perez⁵⁴, S. Roiser³⁸,
 V. Romanovsky³⁵, A. Romero Vidal³⁷, J. W. Ronayne¹², M. Rotondo²², J. Rouvinet³⁹, T. Ruf³⁸,

H. Ruiz³⁶, P. Ruiz Valls⁶⁶, J.J. Saborido Silva³⁷, N. Sagidova³⁰, P. Sail⁵¹, B. Saitta^{15,e}, V. Salustino Guimaraes², C. Sanchez Mayordomo⁶⁶, B. Sanmartin Sedes³⁷, R. Santacesaria²⁵, C. Santamarina Rios³⁷, M. Santimaria¹⁸, E. Santovetti^{24,l}, A. Sarti^{18,m}, C. Satriano^{25,n}, A. Satta²⁴, D.M. Saunders⁴⁶, D. Savrina^{31,32}, M. Schiller³⁸, H. Schindler³⁸, M. Schlupp⁹, M. Schmelling¹⁰, T. Schmelzer⁹, B. Schmidt³⁸, O. Schneider³⁹, A. Schopper³⁸, M. Schubiger³⁹, M.-H. Schune⁷, R. Schwemmer³⁸, B. Sciascia¹⁸, A. Sciubba^{25,m}, A. Semennikov³¹, N. Serra⁴⁰, J. Serrano⁶, L. Sestini²², P. Seyfert²⁰, M. Shapkin³⁵, I. Shapoval^{16,43,f}, Y. Shcheglov³⁰, T. Shears⁵², L. Shekhtman³⁴, V. Shevchenko⁶⁴, A. Shires⁹, B.G. Siddi¹⁶, R. Silva Coutinho⁴⁸, G. Simi²², M. Sirendi⁴⁷, N. Skidmore⁴⁶, I. Skillicorn⁵¹, T. Skwarnicki⁵⁹, E. Smith^{55,49}, E. Smith⁵³, I. T. Smith⁵⁰, J. Smith⁴⁷, M. Smith⁵⁴, H. Snoek⁴¹, M.D. Sokoloff^{57,38}, F.J.P. Soler⁵¹, F. Soomro³⁹, D. Souza⁴⁶, B. Souza De Paula², B. Spaan⁹, P. Spradlin⁵¹, S. Sridharan³⁸, F. Stagni³⁸, M. Stahl¹¹, S. Stahl³⁸, O. Steinkamp⁴⁰, O. Stenyakin³⁵, F. Sterpka⁵⁹, S. Stevenson⁵⁵, S. Stoica²⁹, S. Stone⁵⁹, B. Storaci⁴⁰, S. Stracka^{23,t}, M. Straticiu²⁹, U. Straumann⁴⁰, L. Sun⁵⁷, W. Sutcliffe⁵³, K. Swientek²⁷, S. Swientek⁹, V. Syropoulos⁴², M. Szczekowski²⁸, P. Szczypka^{39,38}, T. Szumlak²⁷, S. T'Jampens⁴, A. Tayduganov⁶, T. Tekampe⁹, M. Teklishyn⁷, G. Tellarini^{16,f}, F. Teubert³⁸, C. Thomas⁵⁵, E. Thomas³⁸, J. van Tilburg⁴¹, V. Tisserand⁴, M. Tobin³⁹, J. Todd⁵⁷, S. Tolk⁴², L. Tomassetti^{16,f}, D. Tonelli³⁸, S. Topp-Joergensen⁵⁵, N. Torr⁵⁵, E. Tournefier⁴, S. Tourneur³⁹, K. Trabelsi³⁹, M.T. Tran³⁹, M. Tresch⁴⁰, A. Trisovic³⁸, A. Tsaregorodtsev⁶, P. Tsopelas⁴¹, N. Tuning^{41,38}, A. Ukleja²⁸, A. Ustyuzhanin^{65,64}, U. Uwer¹¹, C. Vacca^{15,e}, V. Vagnoni¹⁴, G. Valenti¹⁴, A. Vallier⁷, R. Vazquez Gomez¹⁸, P. Vazquez Regueiro³⁷, C. Vázquez Sierra³⁷, S. Vecchi¹⁶, J.J. Velthuis⁴⁶, M. Veltri^{17,h}, G. Veneziano³⁹, M. Vesterinen¹¹, B. Viaud⁷, D. Vieira², M. Vieites Diaz³⁷, X. Vilasis-Cardona^{36,p}, A. Vollhardt⁴⁰, D. Volyanskyy¹⁰, D. Voong⁴⁶, A. Vorobyev³⁰, V. Vorobyev³⁴, C. Voß⁶³, J.A. de Vries⁴¹, R. Waldi⁶³, C. Wallace⁴⁸, R. Wallace¹², J. Walsh²³, S. Wandernoth¹¹, J. Wang⁵⁹, D.R. Ward⁴⁷, N.K. Watson⁴⁵, D. Websdale⁵³, A. Weiden⁴⁰, M. Whitehead⁴⁸, G. Wilkinson^{55,38}, M. Wilkinson⁵⁹, M. Williams³⁸, M.P. Williams⁴⁵, M. Williams⁵⁶, T. Williams⁴⁵, F.F. Wilson⁴⁹, J. Wimberley⁵⁸, J. Wishahi⁹, W. Wislicki²⁸, M. Witek²⁶, G. Wormser⁷, S.A. Wotton⁴⁷, S. Wright⁴⁷, K. Wyllie³⁸, Y. Xie⁶¹, Z. Xu³⁹, Z. Yang³, J. Yu⁶¹, X. Yuan³⁴, O. Yushchenko³⁵, M. Zangoli¹⁴, M. Zavertyaev^{10,b}, L. Zhang³, Y. Zhang³, A. Zhelezov¹¹, A. Zhokhov³¹, L. Zhong³, S. Zucchelli¹⁴.

¹ Centro Brasileiro de Pesquisas Físicas (CBPF), Rio de Janeiro, Brazil

² Universidade Federal do Rio de Janeiro (UFRJ), Rio de Janeiro, Brazil

³ Center for High Energy Physics, Tsinghua University, Beijing, China

⁴ LAPP, Université Savoie Mont-Blanc, CNRS/IN2P3, Annecy-Le-Vieux, France

⁵ Clermont Université, Université Blaise Pascal, CNRS/IN2P3, LPC, Clermont-Ferrand, France

⁶ CPPM, Aix-Marseille Université, CNRS/IN2P3, Marseille, France

⁷ LAL, Université Paris-Sud, CNRS/IN2P3, Orsay, France

⁸ LPNHE, Université Pierre et Marie Curie, Université Paris Diderot, CNRS/IN2P3, Paris, France

⁹ Fakultät Physik, Technische Universität Dortmund, Dortmund, Germany

¹⁰ Max-Planck-Institut für Kernphysik (MPIK), Heidelberg, Germany

¹¹ Physikalisches Institut, Ruprecht-Karls-Universität Heidelberg, Heidelberg, Germany

¹² School of Physics, University College Dublin, Dublin, Ireland

¹³ Sezione INFN di Bari, Bari, Italy

¹⁴ Sezione INFN di Bologna, Bologna, Italy

¹⁵ Sezione INFN di Cagliari, Cagliari, Italy

¹⁶ Sezione INFN di Ferrara, Ferrara, Italy

¹⁷ Sezione INFN di Firenze, Firenze, Italy

- ¹⁸ *Laboratori Nazionali dell'INFN di Frascati, Frascati, Italy*
- ¹⁹ *Sezione INFN di Genova, Genova, Italy*
- ²⁰ *Sezione INFN di Milano Bicocca, Milano, Italy*
- ²¹ *Sezione INFN di Milano, Milano, Italy*
- ²² *Sezione INFN di Padova, Padova, Italy*
- ²³ *Sezione INFN di Pisa, Pisa, Italy*
- ²⁴ *Sezione INFN di Roma Tor Vergata, Roma, Italy*
- ²⁵ *Sezione INFN di Roma La Sapienza, Roma, Italy*
- ²⁶ *Henryk Niewodniczanski Institute of Nuclear Physics Polish Academy of Sciences, Kraków, Poland*
- ²⁷ *AGH - University of Science and Technology, Faculty of Physics and Applied Computer Science, Kraków, Poland*
- ²⁸ *National Center for Nuclear Research (NCBJ), Warsaw, Poland*
- ²⁹ *Horia Hulubei National Institute of Physics and Nuclear Engineering, Bucharest-Magurele, Romania*
- ³⁰ *Petersburg Nuclear Physics Institute (PNPI), Gatchina, Russia*
- ³¹ *Institute of Theoretical and Experimental Physics (ITEP), Moscow, Russia*
- ³² *Institute of Nuclear Physics, Moscow State University (SINP MSU), Moscow, Russia*
- ³³ *Institute for Nuclear Research of the Russian Academy of Sciences (INR RAN), Moscow, Russia*
- ³⁴ *Budker Institute of Nuclear Physics (SB RAS) and Novosibirsk State University, Novosibirsk, Russia*
- ³⁵ *Institute for High Energy Physics (IHEP), Protvino, Russia*
- ³⁶ *Universitat de Barcelona, Barcelona, Spain*
- ³⁷ *Universidad de Santiago de Compostela, Santiago de Compostela, Spain*
- ³⁸ *European Organization for Nuclear Research (CERN), Geneva, Switzerland*
- ³⁹ *Ecole Polytechnique Fédérale de Lausanne (EPFL), Lausanne, Switzerland*
- ⁴⁰ *Physik-Institut, Universität Zürich, Zürich, Switzerland*
- ⁴¹ *Nikhef National Institute for Subatomic Physics, Amsterdam, The Netherlands*
- ⁴² *Nikhef National Institute for Subatomic Physics and VU University Amsterdam, Amsterdam, The Netherlands*
- ⁴³ *NSC Kharkiv Institute of Physics and Technology (NSC KIPT), Kharkiv, Ukraine*
- ⁴⁴ *Institute for Nuclear Research of the National Academy of Sciences (KINR), Kyiv, Ukraine*
- ⁴⁵ *University of Birmingham, Birmingham, United Kingdom*
- ⁴⁶ *H.H. Wills Physics Laboratory, University of Bristol, Bristol, United Kingdom*
- ⁴⁷ *Cavendish Laboratory, University of Cambridge, Cambridge, United Kingdom*
- ⁴⁸ *Department of Physics, University of Warwick, Coventry, United Kingdom*
- ⁴⁹ *STFC Rutherford Appleton Laboratory, Didcot, United Kingdom*
- ⁵⁰ *School of Physics and Astronomy, University of Edinburgh, Edinburgh, United Kingdom*
- ⁵¹ *School of Physics and Astronomy, University of Glasgow, Glasgow, United Kingdom*
- ⁵² *Oliver Lodge Laboratory, University of Liverpool, Liverpool, United Kingdom*
- ⁵³ *Imperial College London, London, United Kingdom*
- ⁵⁴ *School of Physics and Astronomy, University of Manchester, Manchester, United Kingdom*
- ⁵⁵ *Department of Physics, University of Oxford, Oxford, United Kingdom*
- ⁵⁶ *Massachusetts Institute of Technology, Cambridge, MA, United States*
- ⁵⁷ *University of Cincinnati, Cincinnati, OH, United States*
- ⁵⁸ *University of Maryland, College Park, MD, United States*
- ⁵⁹ *Syracuse University, Syracuse, NY, United States*
- ⁶⁰ *Pontifícia Universidade Católica do Rio de Janeiro (PUC-Rio), Rio de Janeiro, Brazil, associated to ²*
- ⁶¹ *Institute of Particle Physics, Central China Normal University, Wuhan, Hubei, China, associated to ³*
- ⁶² *Departamento de Física, Universidad Nacional de Colombia, Bogota, Colombia, associated to ⁸*
- ⁶³ *Institut für Physik, Universität Rostock, Rostock, Germany, associated to ¹¹*
- ⁶⁴ *National Research Centre Kurchatov Institute, Moscow, Russia, associated to ³¹*
- ⁶⁵ *Yandex School of Data Analysis, Moscow, Russia, associated to ³¹*
- ⁶⁶ *Instituto de Física Corpuscular (IFIC), Universitat de Valencia-CSIC, Valencia, Spain, associated to ³⁶*
- ⁶⁷ *Van Swinderen Institute, University of Groningen, Groningen, The Netherlands, associated to ⁴¹*

- ^a *Universidade Federal do Triângulo Mineiro (UFMT), Uberaba-MG, Brazil*
- ^b *P.N. Lebedev Physical Institute, Russian Academy of Science (LPI RAS), Moscow, Russia*
- ^c *Università di Bari, Bari, Italy*
- ^d *Università di Bologna, Bologna, Italy*
- ^e *Università di Cagliari, Cagliari, Italy*
- ^f *Università di Ferrara, Ferrara, Italy*
- ^g *Università di Firenze, Firenze, Italy*
- ^h *Università di Urbino, Urbino, Italy*
- ⁱ *Università di Modena e Reggio Emilia, Modena, Italy*
- ^j *Università di Genova, Genova, Italy*
- ^k *Università di Milano Bicocca, Milano, Italy*
- ^l *Università di Roma Tor Vergata, Roma, Italy*
- ^m *Università di Roma La Sapienza, Roma, Italy*
- ⁿ *Università della Basilicata, Potenza, Italy*
- ^o *AGH - University of Science and Technology, Faculty of Computer Science, Electronics and Telecommunications, Kraków, Poland*
- ^p *LIFAELS, La Salle, Universitat Ramon Llull, Barcelona, Spain*
- ^q *Hanoi University of Science, Hanoi, Viet Nam*
- ^r *Università di Padova, Padova, Italy*
- ^s *Università di Pisa, Pisa, Italy*
- ^t *Scuola Normale Superiore, Pisa, Italy*
- ^u *Università degli Studi di Milano, Milano, Italy*
- ^v *Politecnico di Milano, Milano, Italy*
- [†] *Deceased*